Title: Ocean Acidification and the Permo-Triassic Mass Extinction

Authors: Clarkson, M.O.[1*]; Kasemann, S.A. [2]; Wood, R.[1]; Lenton, T.M.[3]; Daines, S.J.[3]; Richoz, S.[4]; Ohnemueller, F.[2]; Meixner, A.[2]; Poulton, S.W.[5] and Tipper, E.T.[6]

Affiliations:

[1.] School of Geosciences, University of Edinburgh, West Mains Road, Edinburgh, EH9 3JW, UK

[2.] Faculty of Geosciences and MARUM-Center for Marine Environmental Sciences, University of Bremen, 28334 Bremen, Germany

[3.] College of Life and Environmental Sciences, University of Exeter, Laver Building, North Parks Road, Exeter, EX4 4QE, UK.

[4.] Institute of Earth Sciences, University of Graz, Heinrichstraße 26, 8010 Graz, Austria

[5.] School of Earth and Environment, University of Leeds, Leeds, LS2 9JT, UK

[6.] Dept. of Earth Sciences, University of Cambridge, Downing Street, Cambridge, CB2 3EQ, UK

*Correspondence to: matthew.clarkson@otago.ac.nz

Current address: Department of Chemistry, University of Otago, Union Street, Dunedin, 9016, PO Box 56, New Zealand.

Abstract: Ocean acidification triggered by Siberian Trap volcanism has been implicated as a kill mechanism for the Permo-Triassic mass extinction, but evidence for an acidification event remains inconclusive. To address this, we present a high resolution seawater pH record across this interval, utilizing boron isotope data combined with a quantitative modeling approach. In the latest Permian, the alkalinity of the ocean increased, priming the Earth system with a low level of atmospheric CO_2 and a high ocean buffering capacity. The first phase of extinction was

coincident with a slow injection of isotopically light carbon into the atmosphere-ocean, but the ocean was well-buffered such that ocean pH remained stable. During the second extinction pulse, however, a rapid and large injection of carbon overwhelmed the buffering capacity of the ocean, causing an abrupt and short-lived acidification event that drove the preferential loss of heavily calcified marine biota.

One Sentence Summary: Ocean acidification caused the second phase of mass extinction in the Permo-Triassic, due to a rapid and large injection of carbon which overwhelmed the buffering capacity of the ocean.

Main Text: The Permian Triassic Boundary (PTB) mass extinction, at ~ 252 Ma, represents the most catastrophic loss of biodiversity in geological history, and played a major role in dictating the subsequent evolution of modern ecosystems (*1*). The end-Permian extinction event spans ~60 kyrs (*2*) and can be resolved into two distinct marine extinction pulses, with the respective kill mechanisms appearing to be ecologically selective (*3*). The first occurred in the latest Permian (Extinction Pulse 1; EP1) and was followed by an interval of temporary recovery before the second pulse (EP2) which occurred in the earliest Triassic. The direct cause of the mass extinction is widely debated with a diverse range of overlapping mechanisms proposed, including widespread water column anoxia (*4*), euxinia (*5*), global warming (*6*) and ocean acidification (*7*).

Models of PTB ocean acidification suggest that a massive, and rapid, release of CO_2 from Siberian Trap volcanism, acidified the ocean (*7*). Indirect evidence for acidification comes from the interpretation of faunal turnover records (*3, 8*), potential dissolution surfaces (*9*) and Ca

47 isotope data (*7*). A rapid input of carbon is also potentially recorded in the negative carbon
48 isotope excursion (CIE) that characterizes the PTB (*10, 11*) . The interpretation of these records
49 is, however, debated (*12*), and of great importance to understanding the current threat of
50 anthropogenically-driven ocean acidification (*11*).

51 Here, we test the ocean acidification hypothesis by presenting a novel proxy record of
52 ocean pH across the PTB, using the boron isotope composition of marine carbonates ($\delta^{11}B_{carb}$)
53 (SM sections 2 to 4). We then employ a carbon cycle model (SM sections 3 to 5) to explore
54 ocean carbonate chemistry and pH scenarios that are consistent with our $\delta^{11}B$ data and published
55 records of carbon cycle disturbance and environmental conditions. The quantitative model uses
56 previous estimates for background Early Permian conditions (*13*) suggesting either high pCO_2
57 (CO_2*Hi:* ~10 PAL, pH ~7.5 $\delta^{11}B_{SW}$ ~36.8‰), or low pCO_2 (CO_2*Lo:* ~3 PAL, pH ~8, $\delta^{11}B_{SW}$
58 ~34‰) (see SM sections 5 and 6 for further details). Through this combined geochemical,
59 geological and modelling approach we are able to produce an envelope that encompasses the
60 most realistic range in pH, which then allows us to resolve three distinct chronological phases of
61 carbon cycle perturbation, each with very different environmental consequences for the Late
62 Permian-Early Triassic Earth system.

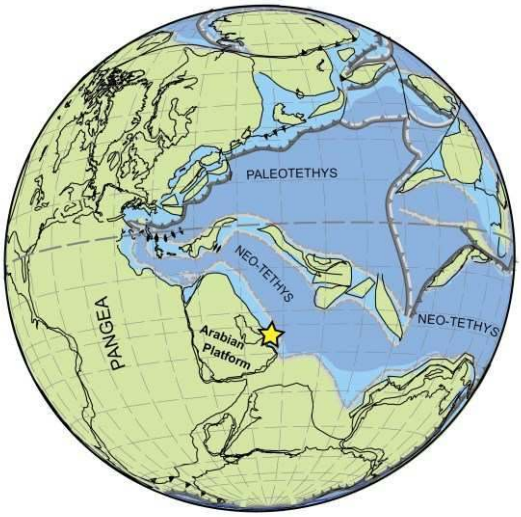

Figure 1

63

Figure 2

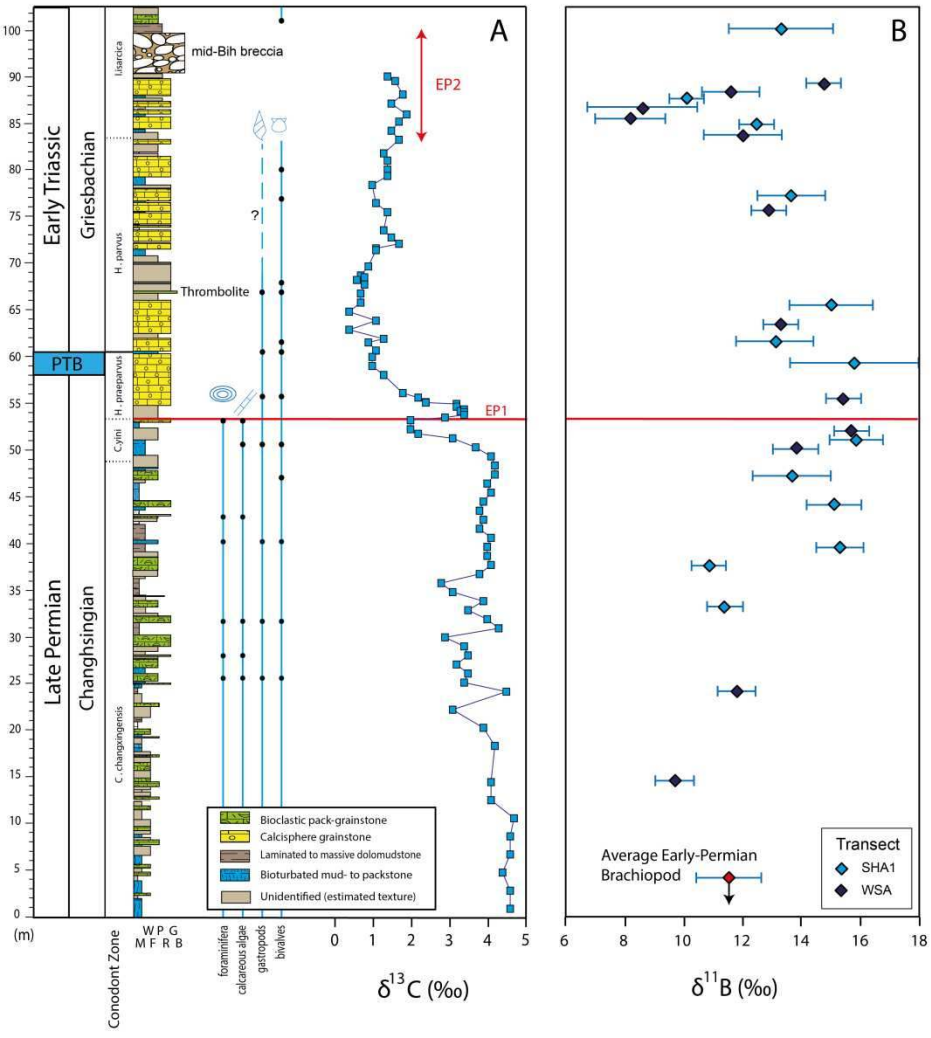

64

65 We analyzed boron isotope data from two complementary transects in a shallow marine,
66 open water carbonate succession from the United Arab Emirates (U.A.E.), where depositional
67 facies and $\delta^{13}C_{carb}$ are well constrained (*14*) (see SM sections 1 and 2). During the Permian-
68 Triassic the U.A.E formed an expansive carbonate platform that remained connected to the
69 central Neo-Tethyan Ocean (*15*) (Fig 1). The run-up to PTB in the Tethys is characterized by
70 two negative $\delta^{13}C$ excursions interrupted by a short-term positive event (*10*). There is no
71 consensus as to the cause of this rebound event and so we focus on the broader $\delta^{13}C$ trend. Our
72 $\delta^{13}C$ transect (Fig. 2) starts in the Changhsingian with a gradual decreasing trend, interrupted by
73 the first negative shift in $\delta^{13}C$ at EP1 (at 53 m or ~251.96 Ma, Fig. 2). This is followed by the
74 minor positive 'rebound' event (at 54 m or ~251.95 Ma, Fig. 2) prior to the minima of the second
75 phase of the negative CIE (58-60 m or ~251.92 Ma, Figs. 2 and 3) that marks the PTB itself.
76 After the CIE minimum, $\delta^{13}C$ gradually increases to ~1.8‰ and remains relatively stable during
77 earliest Triassic and across EP2.

78 Our boron isotope transect shows a quite different pattern. $\delta^{11}B$ is persistently low (Fig. 2),
79 at the start of our record during the late-Changhsingian (Late Permian), with an average of 10.9 ±
80 0.9‰ (1σ). This is in agreement with $\delta^{11}B$ values (average of 10.6 ± 0.6‰, 1σ) reported for
81 early-Permian brachiopods (*16*). Further up section (at ~40 m or ~252.04 Ma, Fig. 2), there is a
82 stepped increase in $\delta^{11}B$ to 15.3‰, and by implication an increase in ocean pH of ~0.4-0.5 pH
83 units (Fig. 3). Then $\delta^{11}B$ values remain relatively stable, scattering around 14.8‰ (± 1.0, 1σ) and
84 implying variations within 0.1-0.2 pH units, into the Early Griesbachian (Early Triassic) and
85 hence across EP1 and the period of carbon cycle disturbance (Figs. 2 and 3).

86 After $\delta^{13}C$ had increased and stabilized (at ~85 m or ~251.88 Ma, Fig. 2), $\delta^{11}B$ begins to
87 decrease rapidly to 8.2‰, implying a sharp drop in pH of ~0.6-0.7 pH units. The $\delta^{11}B$ minimum

Figure 3

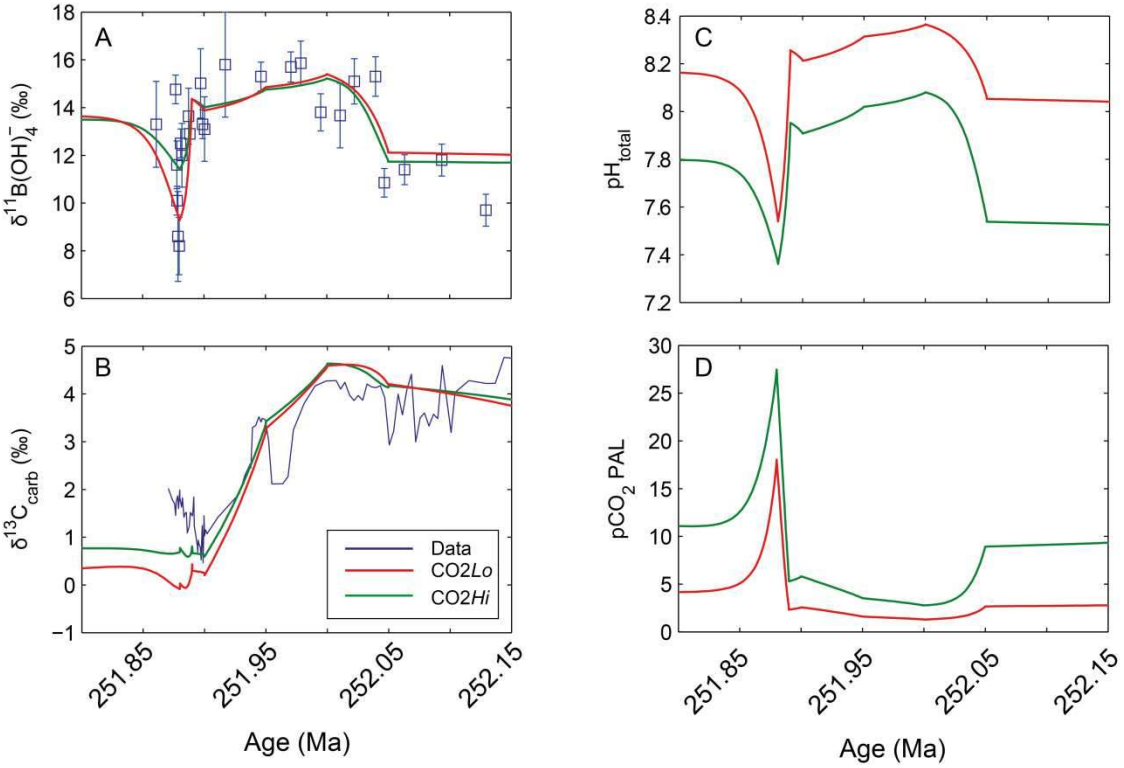

is coincident with the interval identified as EP2. This ocean acidification event is short-lived (~10 kyrs) and $\delta^{11}B$ values quickly recover toward the more alkaline values evident during EP1 (average of ~14‰).

The initial rise in ocean pH of ~0.4-0.5 units during the Late Permian (Fig. 3) suggests a large increase in carbonate alkalinity (*17*). We are able to simulate the observed rise in $\delta^{11}B$ and pH through different model combinations of increasing silicate weathering, increased pyrite deposition (*18*), an increase in carbonate weathering and a decrease in shallow marine carbonate depositional area (see SM section 6.1). Both silicate weathering and pyrite deposition result in a large drop in pCO_2 (and temperature) for a given increase in pH and saturation state (Ω). There is no evidence for a large drop in pCO_2, and independent proxy data indicate only a minor temperature decrease of a few degrees C during the Changsingian *(19)*, suggesting that these mechanisms alone cannot explain the pH increase (see sensitivity tests in SM section 6.1).

Conversely, an increase in carbonate input or a reduction in rates of carbonate deposition both result in increases in Ω, with a greater impact on pH per unit decrease in pCO_2 and temperature (see Fig. S6).

This suggested decrease in carbonate sedimentation is consistent with the decrease in depositional shelf area that occurred due to the 2nd order regression of the Late Permian (*20*). With the added expansion of anoxia into shelf environments (*21*) this would effectively create both bottom-up and top-down pressures to reduce the area of potential carbonate sedimentation. Sea level fall also exposed carbonates to weathering (*20*), which would have further augmented the alkalinity influx. The pH increase event supports the CO_2*Lo* initialisation scenario (CO_2 ~3 PAL, pH ~8, $\delta^{11}B_{SW}$ ~34‰) as the simulated CO_2 and temperature decrease is much reduced, and therefore more consistent with independent proxy data (*22*), compared to CO_2*Hi* (CO_2 ~10 PAL, pH ~7.5 $\delta^{11}B_{SW}$ ~36.8‰) (Fig. 3D).

Prior to EP1, $\delta^{13}C_{carb}$ values begin to decrease before reaching the minimum of the globally recognized negative CIE at the PTB (Fig. 2). At this time both $\delta^{11}B$ and ocean pH remained stable. Hypotheses to explain the negative CIE require the input of isotopically light carbon, such as from volcanism (*14, 23*) with the assimilation of very light organic carbon from the surrounding host rock (*24*), methane destabilization (*22*), collapse of the biological pump (*15*), and/or a decrease in the burial of terrestrial carbon (*16*). We can simulate the observed drop in $\delta^{13}C_{carb}$, whilst remaining within the uncertainty of the $\delta^{11}B$ data (Fig. 3), by combining a cessation of terrestrial carbon burial with a relatively slow (50 kyr) carbon injection from any of the above sources (see section S6.2.4, Fig S8). A small source of methane (3.2×10^{17} mol C with $\delta^{13}C$ = -50‰) gives the least change in $\delta^{11}B$ and pH, whilst either a larger source of organic

carbon (~6.5x10^{17} mol C with $\delta^{13}C$ = -25‰) or a mixture of mantle and lighter carbon sources (~1.3x10^{18} mol C with $\delta^{13}C$ = -12.5‰) are still within the measured uncertainty in $\delta^{11}B$.

This relatively slow carbon addition minimises the tendency for a transient decline in surface ocean pH in an ocean that was already primed with a high Ω and hence high buffering capacity from the Late Permian. The global presence of microbial and abiotic carbonate fabrics after EP1 (Fig. 2) (*25*) are indicative that this high Ω was maintained across the CIE. The carbon injection triggers an increase in pCO_2, temperature and silicate weathering, thereby creating an additional counterbalancing alkalinity flux. This is consistent with independent proxy data (*6*). The alkalinity source may have been further increased through soil loss (*26*), the emplacement of easily-weathered Siberian Trap basalt, or the impact of acid rain (*27*) that would have increased weathering efficiency.

The negative $\delta^{11}B_{carb}$ excursion at 251.88 Ma represents a calculated pH decrease of up to 0.7 pH units. It coincides with the second pulse of the extinction (Fig. 2), which preferentially affected the heavily calcifying, physiologically un-buffered and sessile organisms (*3*). This was also accompanied by the temporary loss of abiotic and microbial carbonates throughout the Tethys (*28, 29*) thereby suggesting a coeval decrease in Ω (*30*). To overwhelm the buffering capacity of the ocean and decrease pH in this way requires a second, more abrupt injection of carbon to the atmosphere, yet remarkably, the acidification event occurs after the decline in $\delta^{13}C$, when $\delta^{13}C$ has rebounded somewhat and is essentially stable (Fig. 2).

Unlike the first carbon injection, the lack of change in $\delta^{13}C$ at this time rules out very ^{13}C-depleted carbon sources, because no counterbalancing strongly ^{13}C-enriched source exists. Instead, it requires a carbon source near ~0‰. A plausible scenario for this is the decarbonation of overlying carbonate host rock, into which the Siberian Traps intruded (*24*) or the direct

assimilation of carbonates and evaporites into the melt (*31*). Host carbonates would have had $\delta^{13}C$ ~+2-4‰, which when mixed with mantle carbon (~-5‰), potentially produces a source near 0‰. We can simulate the sharp drop in pH and stable $\delta^{13}C$ values (Fig. 3) through a large and rapid carbon release of $2x10^{18}$ mol C over 10 kyr (Fig S8). This second rapid carbon release produces a sharp rise in pCO_2 to ~20 PAL and warming of ~15˚C, consistent with the observation of peak temperatures after EP1 (*26*). Initialization of the carbon cycle model under CO_2*Hi* cannot generate the magnitude of $\delta^{11}B$ drop (Fig. 3A) because the non-linear relation between pH and $\delta^{11}B$ fractionation sets a lower limit of $\delta^{11}B$ at ~10‰ in this case (Fig. S3). Thus low initial CO_2 of ~3 PAL in the late Permian (CO_2*Lo*) is more consistent with the data presented here.

The documented acidification event lasted for only ~10 kyrs. This time span is consistent with the modelled timescale required to replenish the ocean with alkalinity, as carbonate deposition is reduced and weathering is increased under higher pCO_2 and global temperatures. Increased silicate weathering rates drive further CO_2 drawdown resulting in stabilization (Fig. S7). High global temperature (*6*) and increased silicate weathering are consistent with a sudden increase in both $^{87}Sr/^{86}Sr$ (*32*) and sedimentation rates (*26*) in the Griesbachian.

The Permo-Triassic transition was a time of extreme environmental change, and our combined data and modeling approach falsifies several mechanisms for the changes observed. Whilst the coincident stresses of anoxia, increasing temperatures, and ecosystem restructuring were important during this interval, the $\delta^{11}B$ excursion strongly suggests that widespread ocean acidification was the driver of the second pulse of the mass extinction, and thus ultimately ended the temporary recovery (*3*) from the first extinction pulse. The carbon release required to drive the observed acidification event occurred at a rate comparable to the current anthropogenic

168 perturbation, but far exceeded it in expected magnitude (*33*). We show that such a rapid rate is
169 critical to causing the combined synchronous decrease in both pH and saturation state that
170 defines an ocean acidification event (*11*).
171
172

References and Notes

1. D. H. Erwin, The Permo-Triassic Extinction. *Nature* **367**, 231-236 (1994).

2. S. D. Burgess, S. A. Bowring, S. Z. Shen, High-precision timeline for Earth's most severe extinction. *Proceedings of the National Academy of Sciences of the United States of America* **111**, 3203-3204 (2014).

3. H. J. Song, P. B. Wignall, J. A. Tong, Y. Hongfu, Two pulses of extinction during the Permian-Triassic crisis. *Nat. Geosci.* **6**, 52-56 (2012).

4. P. B. Wignall, R. J. Twitchett, Oceanic anoxia and the end Permian mass extinction. *Science* **272**, 1155-1158 (1996).

5. K. Grice, C. Q. Cao, G. D. Love, M. E. Bottcher, R. J. Twitchett, E. Grosjean, R. E. Summons, S. C. Turgeon, W. Dunning, Y. G. Jin, Photic zone euxinia during the Permian-Triassic superanoxic event. *Science* **307**, 706-709 (2005); (10.1126/science.1104323).

6. Y. D. Sun, M. M. Joachimski, P. B. Wignall, C. B. Yan, Y. L. Chen, H. S. Jiang, L. N. Wang, X. L. Lai, Lethally Hot Temperatures During the Early Triassic Greenhouse. *Science* **338**, 366-370 (2012); (10.1126/science.1224126).

7. J. L. Payne, A. V. Turchyn, A. Paytan, D. J. DePaolo, D. J. Lehrmann, M. Y. Yu, J. Y. Wei, Calcium isotope constraints on the end-Permian mass extinction. *Proceedings of the National Academy of Sciences of the United States of America* **107**, 8543-8548 (2010); (10.1073/pnas.0914065107).

8. A. H. Knoll, R. K. Barnbach, J. L. Payne, S. Pruss, W. W. Fischer, Paleophysiology and end-Permian mass extinction. *Earth and Planetary Science Letters* **256**, 295-313 (2007); (10.1016/j.epsl.2007.02.018).

9. J. L. Payne, D. J. Lehrmann, D. Follett, M. Seibel, L. R. Kump, A. Riccardi, D. Altiner, H. Sano, J. Wei, Erosional truncation of uppermost Permian shallow-marine carbonates and implications for Permian-Triassic boundary events. *Geol. Soc. Am. Bull.* **119**, 771-784 (2007); (10.1130/b26091.1).

10. C. Korte, H. W. Kozur, Carbon-isotope stratigraphy across the Permian-Triassic boundary: A review. *Journal of Asian Earth Sciences* **39**, 215-235 (2010); (10.1016/j.jseaes.2010.01.005).

11. B. Hönisch, A. Ridgwell, D. N. Schmidt, E. Thomas, S. J. Gibbs, A. Sluijs, R. Zeebe, L. Kump, R. C. Martindale, S. E. Greene, W. Kiessling, J. Ries, J. C. Zachos, D. L. Royer, S. Barker, T. M. Marchitto, Jr., R. Moyer, C. Pelejero, P. Ziveri, G. L. Foster, B. Williams, The Geological Record of Ocean Acidification. *Science* **335**, 1058-1063 (2012); (10.1126/science.1208277).

12. C. L. Blätter, H. C. Jenkyns, L. M. Reynard, G. M. Henderson, Signifcant increases in global weathering during Oceanic Anoxic Events 1a and 2 indicated by calcium isotopes. *Earth and Planetary Science Letters* **309**, 77-88 (2011).

13. Y. Cui, L. R. Kump, Global warming and the end-Permian extinction event: Proxy and modeling perspectives. *Earth-Science Reviews*, (2014); (http://dx.doi.org/10.1016/j.earscirev.2014.04.007).

14. M. O. Clarkson, S. Richoz, R. A. Wood, F. Maurer, L. Krystyn, D. J. McGurty, D. Astratti, A new high-resolution delta C-13 record for the Early Triassic: Insights from the Arabian Platform. *Gondwana Research* **24**, 233-242 (2013); (10.1016/j.gr.2012.10.002).

15. G. M. Stampfli, G. D. Borel, A plate tectonic model for the Paleozoic and Mesozoic constrained by dynamic plate boundaries and restored synthetic oceanic isochrons. *Earth and Planetary Science Letters* **196**, 17-33 (2002); (Pii s0012-821x(01)00588-x10.1016/s0012-821x(01)00588-x).

16. M. M. Joachimski, L. Simon, R. van Geldern, C. Lecuyer, Boron isotope geochemistry of Paleozoic brachiopod calcite: Implications for a secular change in the boron isotope geochemistry of seawater over the Phanerozoic. *Geochimica et Cosmochimica Acta* **69**, 4035-4044 (2005); (10.1016/j.gca.2004.11.017).

17. the alternative way to drive an increase in pH would be through a removal of carbon, however this would be evident in the $\delta^{13}C$ record so we can rule it out.

18. Bacterial Sulfate Reduction (BSR) is a net source of alkalinity if the generated H_2S is buried as pyrite. Pyrite deposition is seen widely in certain setting during the Late Permian to PTB. See SI for further information.

19. M. M. Joachimski, X. L. Lai, S. Z. Shen, H. S. Jiang, G. M. Luo, B. Chen, J. Chen, Y. D. Sun, Climate warming in the latest Permian and the Permian-Triassic mass extinction. *Geology* **40**, 195-198 (2012); (Doi 10.1130/G32707.1).

20. H. Yin, H. Jiang, W. Xia, Q. Feng, N. Zhang, J. Shen, The end-Permian regression in South China and its implication on mass extinction. *Earth-Sci. Rev.* **137**, 19-33 (2014); (http://dx.doi.org/10.1016/j.earscirev.2013.06.003).

21. P. B. Wignall, R. J. Twitchett, Extent, duration, and nature of the Permian-Triassic superanoxic event. *Catastrophic Events and Mass Extinctions: Impacts and Beyond*, 395-413 (2002).

22. E. S. Krull, G. J. Retallack, δ13C depth profiles from paleosols across the Permian-Triassic boundary: Evidence for methane release. *Geol. Soc. Am. Bull.* **112**, 1459-1472 (2000); (10.1130/0016-7606(2000)112%3c;1459:cdpfpa%3e;2.0.co;2).

23. C. Korte, P. Pande, P. Kalia, H. W. Kozur, M. M. Joachimski, H. Oberhaensli, Massive volcanism at the Permian-Triassic boundary and its impact on the isotopic composition of the ocean and atmosphere. *Journal of Asian Earth Sciences* **37**, 293-311 (2010); (10.1016/j.jseaes.2009.08.012).

24. H. Svensen, S. Planke, A. G. Polozov, N. Schmidbauer, F. Corfu, Y. Y. Podladchikov, B. Jamtveit, Siberian gas venting and the end-Permian environmental crisis. *Earth and Planetary Science Letters* **277**, 490-500 (2009); (10.1016/j.epsl.2008.11.015).

25. A. D. Woods, Assessing Early Triassic Paleoceanographic conditions vias unusual sedimentary fabrics and features. *Earth-Sci. Rev.*, (2013); (http://dx.doi.org/10.1016/j.earscirev.2013.08.015).

26. T. J. Algeo, Z. Q. Chen, M. L. Fraiser, R. J. Twitchett, Terrestrial-marine teleconnections in the collapse and rebuilding of Early Triassic marine ecosystems. *Paleogeography Paleoclimatology Paleoecology* **308**, 1-11 (2011); (10.1016/j.paleo.2011.01.011).

27. B. A. Black, J. F. Lamarque, C. A. Shields, L. T. Elkins-Tanton, J. T. Kiehl, Acid rain and ozone depletion from pulsed Siberian Traps magmatism. *Geology* **42**, 67-70 (2014); (Doi 10.1130/G34875.1).

28. A. Baud, S. Richoz, S. Pruss, The lower Triassic anachronistic carbonate facies in space and time. *Global and Planetary Change* **55**, 81-89 (2007); (10.1016/j.gloplacha.2006.06.008).

29. S. Richoz, L. Krystyn, A. Baud, R. Brandner, M. Horacek, P. Mohtat-Aghai, Permian-Triassic boundary interval in the Middle East (Iran and N. Oman): Progressive environmental change from detailed carbonate carbon isotope marine curve and sedimentary evolution. *Journal of Asian Earth Sciences* **39**, 236-253 (2010); (10.1016/j.jseaes.2009.12.014).

30. Note that the system connot be undersaturated as this precludes the preservation of the boron isotope record.

31. B. A. Black, L. T. Elkins-Tanton, M. C. Rowe, I. U. Peate, Magnitude and consequences of volatile release from the Siberian Traps. *Earth and Planetary Science Letters* **317**, 363-373 (2012); (Doi 10.1016/J.Epsl.2011.12.001).

32. C. Korte, H. W. Kozur, M. M. Joachimski, H. Strauss, J. Veizer, L. Schwark, Carbon, sulfur, oxygen and strontium isotope records, organic geochemistry and biostratigraphy across the Permian/Triassic boundary in Abadeh, Iran. *International Journal of Earth Sciences* **93**, 565-581 (2004); (Doi 10.1007/S00531-004-0406-7).

33. The imposed perturbation for the acidification event is 24000 PgC compared to the estimates of 4-5000PgC that could be generated from conventional fossil fuels. Upper estimates using unconvential fossil fuels (e.g. methane hydrates) can reach ~ 24000 PgC

34. F. Maurer, R. Martini, R. Rettori, H. Hillgartner, S. Cirilli, The geology of Khuff outcrop analogues in the Musandam Peninsula, United Arab Emirates and Oman. *GeoArabia* **14**, 125-158 (2009).

35. S. Z. Shen, C. Q. Cao, H. Zhang, S. A. Bowring, C. M. Henderson, J. L. Payne, V. I. Davydov, B. Chen, D. X. Yuan, Y. C. Zhang, W. Wang, Q. F. Zheng, High-resolution delta C-13(carb) chemostratigraphy from latest Guadalupian through earliest Triassic in South China and Iran. *Earth and Planetary Science Letters* **375**, 156-165 (2013); (Doi 10.1016/J.Epsl.2013.05.020).

36. B. Koehrer, M. Zeller, T. Aigner, M. Poeppelreiter, P. Milroy, H. Forke, S. Al-Kindi, Facies and stratigraphic framework of a Khuff outcrop equivalent: Saiq and Mahil formations, Al Jabal al-Akhdar, Sultanate of Oman. *GeoArabia* **15**, 91-156 (2010).

37. S. Kasemann, A. Meixner, A. Rocholl, T. Vennemann, M. Rosner, A. K. Schmitt, M. Wiedenbeck, Boron and oxygen isotope composition of certified reference materials NIST SRM 610/612 and reference materials JB-2 and JR-2. *Geostandards Newsletter-the Journal of Geostandards and Geoanalysis* **25**, 405-416 (2001); (Doi 10.1111/J.1751-908x.2001.Tb00615.X).

38. J. Vogl, M. Rosner, W. Pritzkow, Development and validation of a single collector SF-ICPMS procedure for the determination of boron isotope ratios in water and food samples. *Journal of Analytical Atomic Spectrometry*, **26**, 861-869 (2011).

39. S. A. Kasemann, SD. N. Schmidt, J. Bijma, J., G. L. Foster, In situ boron isotope analysis in marine carbonates and its application for foraminifera and paleo-pH.*Chemical Geology,*. **260,** 138-147 (2009)

40. S. A. Kasemann, C. J. Hawkesworth, A. R. Prave, A. E. Fallick, P. N. Pearson, Boron and calcium isotope composition in Neoproterozoic carbonate rocks from Namibia: evidence for extreme environmental change. *Earth and Planetary Science Letters* **231**, 73-86 (2005); (Doi 10.1016/J.Epsl.2004.12.006).

41. F. Ohnemüller, A. R. Prave, A. E. Fallick, S. A. Kasemann, Ocean acidification in the aftermath of the Marinoan glaciation. *Geology,* doi:10.1130/G35937.1 (2014).

42. P. B. Wignall, A. Hallam, Facies change and the end-Permian mass extinction in SE Sichuan, China. *Palaios* **11**, 587-596 (1996).

43. L. Breesch, R. Swennen, B. Dewever, F. Roure, B. Vincent, Diagenesis and fluid system evolution in the northern Oman Mountains, United Arab Emirates: Implications for petroleum exploration. *GeoArabia* **16**, 111-148 (2011).

44. S. B. Jacobsen, A. J. Kaufman, The Sr, C and O isotopic evolution of Neoproterozoic seawater. *Chem. Geol.* **161**, 37-57 (1999); (Doi 10.1016/S0009-2541(99)00080-7).

45. S. A. Kasemann, A. R. Prave, A. E. Fallick, C. J. Hawkesworth, K. H. Hoffmann, Neoproterozoic ice ages, boron isotopes, and ocean acidification: Implications for a snowball Earth. *Geology* **38**, 775-778 (2010); (10.1130/g30851.1).

46. G. Paris, A. Bartolini, Y. Donnadieu, V. Beaumont, J. Gaillardet, Investigating boron isotopes in a middle Jurassic micritic sequence: Primary vs. diagenetic signal. *Chem. Geol.* **275**, 117-126 (2010); (10.1016/j.chemgeo.2010.03.013).

47. A. J. Spivack, J. M. Edmond, Boron Isotope Exchange between Seawater and the Oceanic-Crust. *Geochimica et Cosmochimica Acta* **51**, 1033-1043 (1987); (Doi 10.1016/0016-7037(87)90198-0).

48. J. Veizer, D. Ala, K. Azmy, P. Bruckschen, D. Buhl, F. Bruhn, G.A. F. Carden, A. Diener, S. Ebneth, Y. Godderis, T. Jasper, C. Korte, F. Pawellek, O. Podlaha, and Strauss, H. "$^{87}Sr/^{86}Sr$, $\delta^{13}C$ and $\delta^{18}O$ evolution of Phanerozoic seawater". *Chemical Geology* **161**: 59-88 (1999).

49. D. Lemarchand, J. Gaillardet, E. Lewin, C. J. Allegre, The influence of rivers on marine boron isotopes and implications for reconstructing past ocean pH. *Nature* **408**, 951-954 (2000).

50. A. G. Dickson, Thermodynamics of the dissociation of boric-acid in synthetic seawater from 273.15-k to 318.15-k. *Deep-Sea Research Part a-Oceanographic Research Papers* **37**, 755-766 (1990).

51. M. Schobben, M. M. Joachimski, D. Korn, L. Leda, C. Korte, Paleotethys seawater temperature rise and an intensified hydrological cycle following the end-Permian mass extinction. *Gondwana Research*, (2013); (http://dx.doi.org/10.1016/j.gr.2013.07.019).

52. J. T. Kiehl, C. A. Shields, Climate simulation of the latest Permian: Implications for mass extinction. *Geology* **33**, 757-760 (2005); (Doi 10.1130/G21654.1).

53. R. A. Locarnini, A. V. Mishonov, J. I. Antonov, T. P. Boyer, H. E. Garcia, in *NOAA Atlas NESDIS 61,* S. Levitus, Ed. (U.S. Government Printing Office, Washington, D.C, 2006), vol. 1: Temperature.

54. P. N. Pearson, M. R. Palmer, Atmospheric carbon dioxide concentrations over the past 60 million years. *Nature* **406**, 695-699 (2000).

55. G. L. Foster, Seawater pH, PCO2 and [CO32-] variations in the Caribbean Sea over the last 130 kyr: A boron isotope and B/Ca study of planktic forminifera. *Earth and Planetary Science Letters* **271**, 254-266 (2008); (10.1016/j.epsl.2008.04.015).

56. B. Hönisch, N. G. Hemming, D. Archer, M. Siddall, J. F. McManus, Atmospheric Carbon Dioxide Concentration Across the Mid-Pleistocene Transition. *Science* **324**, 1551-1554 (2009); (Doi 10.1126/Science.1171477).

57. N. G. Hemming, G. N. Hanson, Boron isotopic composition and concentration in modern marine carbonates. *Geochimica et Cosmochimica Acta* **56**, 537-543 (1992).

58. N. G. Hemming, B. Honisch, A critical review and recent advances in the boron isotope paleo-pH proxy. *Geochimica et Cosmochimica Acta* **69**, A129-A129 (2005).

59. K. Klochko, A. J. Kaufman, W. S. Yao, R. H. Byrne, J. A. Tossell, Experimental measurement of boron isotope fractionation in seawater. *Earth and Planetary Science Letters* **248**, 276-285 (2006); (10.1016/j.epsl.2006.05.034).

60. E. Lewis, D. W. R. Wallace. (Oak Ridge, 1998).

61. J. W. B. Rae, G. L. Foster, D. N. Schmidt, T. Elliott, Boron isotopes and B/Ca in benthic foraminifera: Proxies for the deep ocean carbonate system. *Earth and Planetary Science Letters* **302**, 403-413 (2011).

62. M. Pagani, J. C. Zachos, K.H. Freeman, B. Tipple, H. Bohaty, Marked decline in atmospheric carbon dioxide concentrations during the Paleogene. *Science* **309**, 600-603 (2005)

63. A. Sanyal, M. Nugent, R. J. Reeder, J. Buma, Seawater pH control on the boron isotopic composition of calcite: Evidence from inorganic calcite precipitation experiments. *Geochimica et Cosmochimica Acta* **64**, 1551-1555 (2000).

64. K. Klochko, G. D. Cody, J. A. Tossell, P. Dera, A. J. Kaufman, Re-evaluating boron speciation in biogenic calcite and aragonite using B-11 MAS NMR. *Geochimica et Cosmochimica Acta* **73**, 1890-1900 (2009); (10.1016/j.gca.2009.01.002).

65. R. A. Berner, Examination of hypotheses for the Permo-Triassic boundary extinction by carbon cycle modeling. *Proceedings of the National Academy of Sciences of the United States of America* **99**, 4172-4177 (2002); (10.1073/pnas.032095199).

66. M. R. Rampino, K. Caldeira, Major perturbation of ocean chemistry and a 'Strangelove Ocean' after the end-Permian mass extinction. *Terra Nova* **17**, 554-559 (2005); (10.1111/j.1365-3121.2005.00648.x).

67. J. Payne, L. Kump, Evidence for recurrent Early Triassic massive volcanism from quantitative interpretation of carbon isotope fluctuations. *Earth and Planetary Science Letters* **256**, 264-277 (2007); (10.1016/j.epsl.2007.01.034).

68. K. Caldeira, J. F. Kasting, The life span of the biosphere revisited. *Nauture* **360**, 721-723 (1992).

69. J. M. Bergman, T. M. Lenton, A. J. Watson, COPSE: A new model of biogeochemical cycling over Phanerozoic time. *American Journal of Science* **304**, (2004).

70. A. F. Hofmann, K. Soetaert, J. J. Middelburg, F. J. R. Meysman, AquaEnv : An Aquatic Acid–Base Modelling Environment in R. *Aquatic Geochemistry* **16**, 507-546 (2010); (10.1007/s10498-009-9084-1).

71. R. E. Zeebe, P. Westbrooke, A simple model for the CaCO3 saturation state of the ocean: The ''Strangelove,'' the ''Neritan,'' and the ''Cretan'' Ocean. *Geochemistry Geophysics Geosystems* **4**, (2003).

72. J. Zhang, P. D. Quay, D. O. Wilbur, Carbon isotope fractionation during gas-water exchange and dissolution of CO2. *Geochimica et Cosmochimica Acta* **59**, 107-114 (1995).

73. H. D. Holland, in *Treatise on Geochemistry: Vol 6 The oceans and marine geochemistry,* H. D. Holland, K. K. Turekian, Eds. (Elsevier Academic Press, 2003), pp. 583-625.

74. H. Song, J. Tong, T. J. Algeo, H. Song, H. Qiu, Y. Zhu, L. Tian, S. Bates, T. W. Lyons, G. Luo, L. R. Kump, Early Triassic seawater sulfate drawdown. *Geochimica et Cosmochimica Acta* **128**, 95-113 (2014); (10.1016/j.gca.2013.12.009).

75. G. Luo, L. R. Kump, Y. Wang, J. Tong, M. a. Arthur, H. Yang, J. Huang, H. Yin, S. Xie, Isotopic evidence for an anomalously low oceanic sulfate concentration following end-Permian mass extinction. *Earth and Planetary Science Letters* **300**, 101-111 (2010); (10.1016/j.epsl.2010.09.041).

76. S. Ben-Yaakov, M. B. Goldhaber, The influence of sea water composition on the apparent constants of the carbonate system. *Deep Sea Research and Oceanographic Abstracts* **20**, 87-99 (1973); (10.1016/0011-7471(73)90044-2).

77. R. E. Zeebe, LOSCAR: Long-term Ocean-atmosphere-Sediment CArbon cycle Reservoir Model v2.0.4. *Geoscientific Model Development* **5**, 149-166 (2012); (10.5194/gmd-5-149-2012).

78. Y. Cui, L. R. Kump, Global warming and the end-Permian extinction event: Proxy and modeling perspectives. (2014); (doi:10.1016/j.earscirev.2014.04.007).

79. Y. Cui, L. R. Kump, A. Ridgwell, Initial assessment of the carbon emission rate and climatic consequences during the end-Permian mass extinction. *Paleogeography Paleoclimatology Paleoecology* **389**, 128-136 (2013).

80. T. J. Algeo, K. Kuwahara, H. Sano, S. Bates, T. Lyons, E. Elswick, L. Hinnov, B. Ellwood, J. Moser, J. B. Maynard, Spatial variation in sediment fluxes, redox conditions, and productivity in the Permian–Triassic Panthalassic Ocean. *Paleogeography, Paleoclimatology, Paleoecology* **308**, 65-83 (2011); (10.1016/j.paleo.2010.07.007).

81. T. J. Algeo, R. J. Twitchett, Anomalous Early Triassic sediment fluxes due to elevated weathering rates and their biological consequences. *Geology* **38**, 1023-1026 (2010); (10.1130/g31203.1).

82. G. A. Brennecka, A. D. Herrmann, T. J. Algeo, A. D. Anbar, Rapid expansion of oceanic anoxia immediately before the end-Permian mass extinction. *Proceedings of the National Academy of Sciences of the United States of America* **108**, 17631-17634 (2011); (10.1073/pnas.1106039108).

83. S. E. Grasby, B. Beauchamp, Latest Permian to Early Triassic basin-to-shelf anoxia in the Sverdrup Basin, Arctic Canada. *Chem. Geol.* **264**, 232-246 (2009); (Doi 10.1016/J.Chemgeo.2009.03.009).

84. C. Winguth, A. M. E. Winguth, Simulating Permian-Triassic oceanic anoxia distribution: Implications for species extinction and recovery. *Geology* **40**, 127-130 (2012); (10.1130/g32453.1).

85. T. J. Algeo, C. M. Henderson, J. N. Tong, Q. L. Feng, H. F. Yin, R. V. Tyson, Plankton and productivity during the Permian-Triassic boundary crisis: An analysis of organic carbon fluxes. *Global and Planetary Change* **105**, 52-67 (2013); (Doi 10.1016/J.Gloplacha.2012.02.008).

86. E. Tziperman, I. Halevy, D. T. Johnston, A. H. Knoll, D. P. Schrag, Biologically induced initiation of Neoproterozoic snowball-Earth events. *Proceedings of the National Academy of Sciences of the United States of America*, 1-6 (2011); (10.1073/pnas.1016361108).

87. S. W. Poulton, D. E. Canfield, Ferruginous Conditions: A Dominant Feature of the Ocean through Earth's History. *Elements* **7**, 107-112 (2011); (10.2113/gselements.7.2.107).

88. H. Song, J. Tong, T. J. Algeo, H. Song, H. Qiu, Y. Zhu, L. Tian, S. Bates, T. W. Lyons, G. Luo, L. R. Kump, Early Triassic seawater sulfate drawdown. *Geochimica et Cosmochimica Acta*, (2013); (doi: http://dx.doi.org/10.1016/j.gca.2013.12.009).

89. W. S. Broecker, S. Peacock, An ecologic explanation for the Permo-Triassic carbon and sulfur isotope shifts. *Global Biogeochemical Cycles* **13**, 1167-1172 (1999).

90. G. Luo, Y. Wang, K. Grice, S. Kershaw, T. J. Algeo, X. Ruan, H. Yang, C. Jia, S. Xie, Microbial–algal community changes during the latest Permian ecological crisis: Evidence from lipid

biomarkers at Cili, South China. *Global and Planetary Change* **105**, 36-51 (2013); (10.1016/j.gloplacha.2012.11.015).

91. K. M. Meyer, M. Yu, A. B. Jost, B. M. Kelley, J. L. Payne, $\delta^{13}C$ evidence that high primary productivity delayed recovery from end-Permian mass extinction. *Earth and Planetary Science Letters* **302**, 378-384 (2011); (10.1016/j.epsl.2010.12.033).

92. H. J. Song, J. N. Tong, Y. L. Xiong, D. Y. Sun, L. Tian, H. Y. Song, The large increase of δ13C(carb)-depth gradient and the end-Permian mass extinction. *Sci. China-Earth Sci.* **55**, 1101-1109 (2012); (10.1007/s11430-012-4416-1).

93. D. E. Ogden, N. H. Sleep, Explosive eruption of coal and basalt and the end-Permian mass extinction. *Proceedings of the National Academy of Sciences of the United States of America* **109**, 59-62 (2012); (10.1073/pnas.1118675109).

94. M. K. Reichow, A. D. Saunders, R. V. White, M. S. Pringle, A. I. Al'Mukhamedov, A. I. Medvedev, N. P. Kirda, Ar-40/Ar-39 dates from the West Siberian Basin: Siberian flood basalt province doubled. *Science* **296**, 1846-1849 (2002).

95. M. B. Harfoot, J. a. Pyle, D. J. Beerling, End-Permian ozone shield unaffected by oceanic hydrogen sulphide and methane releases. *Nat. Geosci.* **1**, 247-252 (2008); (10.1038/ngeo154).

96. C. Ganino, N. T. Arndt, Climate changes caused by degassing of sediments during the emplacement of large igneous provinces. *Geology* **37**, 323-326 (2009); (10.1130/G25325A.1).

Acknowledgements: MOC acknowledges funding from the Edinburgh University Principal's Career Development Scholarship and the International Centre for Carbonate Reservoirs. RW, TL and SWP acknowledge support from NERC through the 'Co-evolution of Life and the Planet' scheme (NE/I005978). SK and FO acknowledge support from the DFG. This is a contribution to IGCP 572 with S.R. sponsored for fieldwork by the Austrian National Committee (Austrian Academy of Sciences) for IGCP. We are grateful to Rob Newton and Alex Thomas for helpful discussions, Leo Krystyn for field assistance, Florian Maurer for providing photomicrographs, and Ben Mills for assisting with model studies.

Fig. 1: Paleogeographic reconstruction for the Late Permian denoting the studied section Wadi Bih, in the Musandam Mountians of U.A.E that formed an extensive carbonate platform in the Neo-Tethyan Ocean. Modified from (*14*).

Fig. 2: Carbon cycle dynamics, macrofauna distribution (*34*), and Extinction Phase 1 (EP1) and Extinction Phase 2 interval (EP2) across the Permian Triassic Boundary for Wadi Bih, A: shallow water $\delta^{13}C$ record (*14*); B: Boron isotope ($\delta^{11}B$) record (propagated uncertainty given as $2\sigma f$) and average Early Permian brachiopod value (n=5) (*16*). Blue symbols are for SHA1 transect, black symbols are for WSA transect. The two transects are separated by ~ 1km and facies are laterally continuous. Only *H. parvus* has been found so far in this section and the conodont zones with dashed line are identified from the $\delta^{13}C$ record (*34-36*).

Fig. 3: Model results of carbon cycle parameters for the two end-member CO_2 scenarios (CO_2*Hi* and CO_2*Lo*). A - Model reproduced $\delta^{11}B$ vs data. B – Modelled $\delta^{13}C$ vs data. C – Modelled pH

480 envelope incorporating uncertainty of $\delta^{11}B_{SW}$ and dynamic temperatures. D – calculated

481 atmospheric CO_2. See SM section 1.2 for details on age model.

482

483

Supplementary Materials:

Materials and Methods

Figures S1-S9

Tables S1-S10

References (*37-96*)

Supplementary Materials

1. Materials and Methods

1.1 Sample Section

Carbonate samples were obtained from a shallow-marine platform section at Wadi Bih on the Musandam Peninsula, United Arab Emirates (UAE). GPS co-ordinate for main transect in Wadi Shahha are N 025° 50′ 31.7″, E 056° 06′ 41.7″**.** This is a near-continuous and exclusively shallow marine carbonate succession from the late Permian and entire Early Triassic that allows analysis of a high-resolution signature in the absence of significant depth-dependent or lithological controls (*14*). Late Permian facies are predominantly intertidal mud-and-wackestones and open lagoon wackestones, occasional windward and leeward shoals of bioclastic pack-and-grainstones (*34*). The PTB and Early Triassic are regionally represented by ooidal grainstones and a thrombolite horizon (*14, 34*). Samples were taken from two transects Wadi Shahha (WSA) and Sha (SHA1), ~1000 m apart.. Facies are laterally continuous and carbon isotopes were used to ensure careful integration of the two datasets. For this study, we have analyzed 25 carbonate samples in total, taken in approximately 1 to 10 m scale intervals and covering a total thickness of 98 m, starting in the mid-Changhsingian (Permian), going up into the mid-Griesbachian (Triassic) and bracketing the complete Permian Triassic Boundary (PTB) extinction event (Table S1).

Table S1: Boron, carbon and oxygen isotope data from Wadi Bih; U.A.E.; pH values are derived from a simplified and non-dynamic calulation using the $\delta^{11}B_{SW}$ range given by the model calculation and a constant pK_B for 25°C, 35 psu, 0 dbar.

Sample	Height (m)	Lithology	Age (Ma)*	$\delta^{13}C$ (‰)	$\delta^{18}O$ (‰)	$\delta^{11}B$ (‰)$^{+}$	2σf (‰)$^{\#}$	pH $\delta^{11}B_{SW}$ 34‰	pH $\delta^{11}B_{SW}$ 36.8‰
Wadi Bih (25° 50' 31.2"N 56° 06' 41.7"E)									
WSA54	14.0	micritic mudstone	252.13	4.20	-2.40	9.7(3)	0.7	7.7	6.7
WSA49	24.0	micritic mudstone	252.09	4.60	-0.50	11.8(3)	0.7	8.0	7.6
SHA1 1	32.4	dolograinstone	252.06	4.23	-3.19	11.4(2)	0.6	7.9	7.5
SHA1 3	37.0	grainstone	252.05	4.22	-2.62	10.8(0)	0.6	7.9	7.4
SHA1 4	39.0	micritic mudstone	252.04	4.26	-2.51	15.3(6)	0.8	8.3	8.1
SHA1 7	43.8	bioclastic packstone	252.02	3.63	-2.65	15.1(7)	1.0	8.3	8.0
SHA1 8	47.0	bioclastic packstone	252.01			13.7(12)	1.4	8.2	7.9
WSA22a	50.0	micritic mudstone	252.00	3.80	-3.50	13.8(5)	0.8	8.2	7.9
SHA1 11	51.0	bioturbated mudston	251.98			15.9(7)	0.9	8.3	8.1
WSA21	52.0	micritic mudstone	251.97	2.10	-4.00	15.7(2)	0.6	8.3	8.1
WSA 17	55.0	micritic mudstone	251.95	2.54	-3.65	15.3(2)	0.6	8.3	8.1
SHA1 15	59.6	calcisphere grainston	251.92	0.52	-3.15	15.8(21)	2.2	8.3	8.1
SHA1 17	62.0	calcisphere grainston	251.90			13.1(12)	1.4	8.1	7.8
WSA12A	64.0	micritic mudstone	251.90	0.50	-3.40	13.3(0)	0.6	8.1	7.8
SHA1 20	66.0	calcisphere grainston	251.90			15.0(13)	1.5	8.3	8.0
WSA5A	77.0	micritic mudstone	251.89	1.50	-3.20	12.9(0)	0.6	8.1	7.8
SHA1 26	78.2	calcisphere grainston	251.89	1.21	-2.55	13.6(10)	1.2	8.2	7.9
WSA3	85.0	micritic mudstone	251.88	1.60	-2.60	12.0(12)	1.3	8.0	7.6
SHA1 30	86.2	calcisphere grainston	251.88			12.5(6)	0.6	8.1	7.7
WSA 2A	86.8	micritic mudstone	251.88	1.99	-2.96	8.2(10)	1.2	7.4	-
WSA2	88.0	micritic mudstone	251.88	1.60	-2.94	8.6(18)	1.9	7.5	< 7,0
WSA 1B	89.0	micritic mudstone	251.88	1.87	-3.26	10.1(2)	0.6	7.8	7.0
SHA1 32	90.2	calcisphere grainston	251.88	1.39	-3.40	11.6(8)	1.0	8.0	7.6
WSA1	91.0	micritic mudstone	251.88	1.46	-3.74	14.8(0)	0.6	8.2	8.0
SHA1 36	102.0	bioclastic packstone	251.86	1.79	-2.00	13.3(17)	1.8	8.1	7.8

* Ages are calculated based on tie points from Burgess et al.(2), see section S1.2

$^{+}$ external uncertainty for B isotope data are valid for the last digits (2σ)

$^{\#}$ propagated uncerteinties for B isotope data

1.2 Age Model

The age model for this study was based on the most recent findings of Burgess et al., (*2*) (see Table S1). The age tie points are 252.10 Ma for 20 m (Fig. 2) thought to be equivalent to Bed 22 in Meishan from the $\delta^{13}C$ record; 252.00 Ma for the decline in $\delta^{13}C$ at 49 m and 251.90 Ma for the first occurrence of *H. parvus* at 61m. EP2 is known to occur at the end of the *I. staeschi* zone, Bed 28 Meishan (*3*), which is not recorded in the Neo-Tethys but is equivalent to the carbon

516 isotope rise between the *H. Parvus* and *I. isarcica* zones. In Wadi Bih we see the loss of
517 gastropods and bivalves at this point (*34*), however the full resolution of the second extinction
518 phase has not been confirmed at this locality. Therefore we identify a 10 m interval for EP2. In
519 order to complete the age model we set the mid-point of EP2 as 251.88 Ma based on the absolute
520 age for EP2 in Meishan (*2*).
521
522 **1.3 Analytical methods**
523 Carbon and oxygen isotope ratios were determined at Edinburgh University and University of
524 Graz using the preparation technique and measurement routine as detailed in (*19*). All carbonate
525 isotopic values are quoted in the conventional δ per mil (‰) notation relative to VPDB.
526 Calibration to international reference material was through NBS 19 and the reproducibility of
527 replicate analyses for reference material, standards (in-house) and carbonate samples was better
528 than ±0.05 ‰ for $\delta^{13}C$ and ±0.1 ‰ for $\delta^{18}O$ at one standard deviation. For a detailed discussion
529 of the C and O isotopic data see (*19*).
530 Boron isotope ratios were determined in the isotope geochemistry laboratory at the
531 University of Bremen (Department of Geosciences and MARUM-Center for Marine
532 Environmental Sciences) using a ThermoFisher Scientific TRITON Plus Thermal Ionization
533 Mass Spectrometer. The $n(^{11}B)/n(^{10}B)$ measurements were performed using negative thermal
534 ionization mass spectrometry (N-TIMS) following the method detailed in (*37*). For analyses, 10
535 mg of the sample powder was dissolved in 100 µl 1 N HCl for 24 h at 20°C and subsequently
536 centrifuged. 1 µl boron-free seawater emitter (*38*) together with 1 µl of the sample solution
537 containing ~1 ng B were placed and dried on a degassed Re single filament. Analyses were
538 carried out at filament temperatures of 970°-1050°C. Boron isotopes were registered as BO_2^-

539 complexes on masses 42 and 43, and measurements were carried out at ion beam intensity of ~
540 10 pA on mass 43. Each sample measurement involved up to 200 blocks with 10 cycles each,
541 taking about 2 hours of data acquisition. B isotope ratios are given relative to NIST SRM 951 in
542 the conventional $\delta^{11}B$ (‰) notation. The external reproducibility of the certified reference
543 material NIST SRM 951 showed an $n(^{11}B)/n(^{10}B)$ ratio of 4.0065±0.0017 (2σ = 0.42‰, n=23)
544 over a period of 6 month of sample analyses. The long term (18 month) reproducibility is
545 4.0066±0.0018 (2σ = 0.44‰, n=58). The $n(^{11}B)/n(^{10}B)$ ratio of the reference material for each
546 analytical session was reproduced better than 0.6‰ (2σ). In addition to the NIST material, the
547 standard material M93-TB-FC-1, a *Porites* coral with a published value of 24.8±0.4‰ ($2\sigma_{mean}$),
548 as determined by different multicollector techniques (*39*) was also regularly analysed. The coral
549 replicates gave $\delta^{11}B$ values of 24.1±0.7‰ (2σ, n=16). Each sample solution was as a minimum
550 run in full duplicate and the uncertainty of the reference material was propagated into the
551 external uncertainty (2σ) on the isotope ratio of the sample ($2\sigma f$; Table S1). For further
552 information on the preparation and analytical methods see (*40*).
553
554 **2. Sample Selection**
555 A critical issue in using the B isotope composition of Permo-Triassic carbonate rocks for
556 reconstruction of ocean pH is the potential overprinting of the original isotope signal via
557 alteration. To obtain high-quality samples in which primary B isotope signals are still preserved,
558 we applied the sample selection procedures successfully used on Neoproterozoic carbonate rocks
559 to reconstruct Cryogenian and Ediacaran ocean pH variation *(37, 40, 41)*. In brief, samples
560 selected for isotope analyses were screened macroscopic (in the field), microscopic (scanning
561 electron microscope) and geochemically (carbon and oxygen isotopes), and selected because of

562 their uniformity in texture, absence of late stage secondary alteration and no correlation between
563 carbon and boron with oxygen isotopic signatures (Figs. S1 and S2).

564 The PTB interval itself was thought to occur in a regional cross-bedded ooid grainstone,
565 however, reconsideration of published thin-section images (*34*) (Fig S1 samples from WSA
566 transect, 0611300847 and 0611181243) demonstrate these are in fact microspheres (a.k.a
567 calcispheres). This fabric is unusual for the Phanerozoic but appears to represent supersaturated
568 conditions and these are thought to be primary spar precipitates (*42*).

569 To gain the highest potential for recording a primary boron signature we microdrilled
570 areas of pure micrite from micritc mudstones and micritised calcisphere grainstones where there
571 was no micro-optical evidence for veining, fracturing, clay minerals or bioclastic material.
572 Samples containing evidence of late stage secondary alteration or recrystallization, i.e. any
573 spar/microspar, were discarded. Potential analyses of disseminated detrital material in the
574 carbonates was also checked through elevated Al, Si and Ba concentrations and showed either no
575 or only minor dissemination of clay. The low availability of bioclastic material in this interval,
576 due to the extinction, argues against the potential of trends being caused by vital effects. In
577 particular the calcisphere grainstones of the PTB interval are classed as an abiotic carbonate that
578 provides an excellent opportunity to record seawater $\delta^{11}B$ in the absence of vital effects.
579

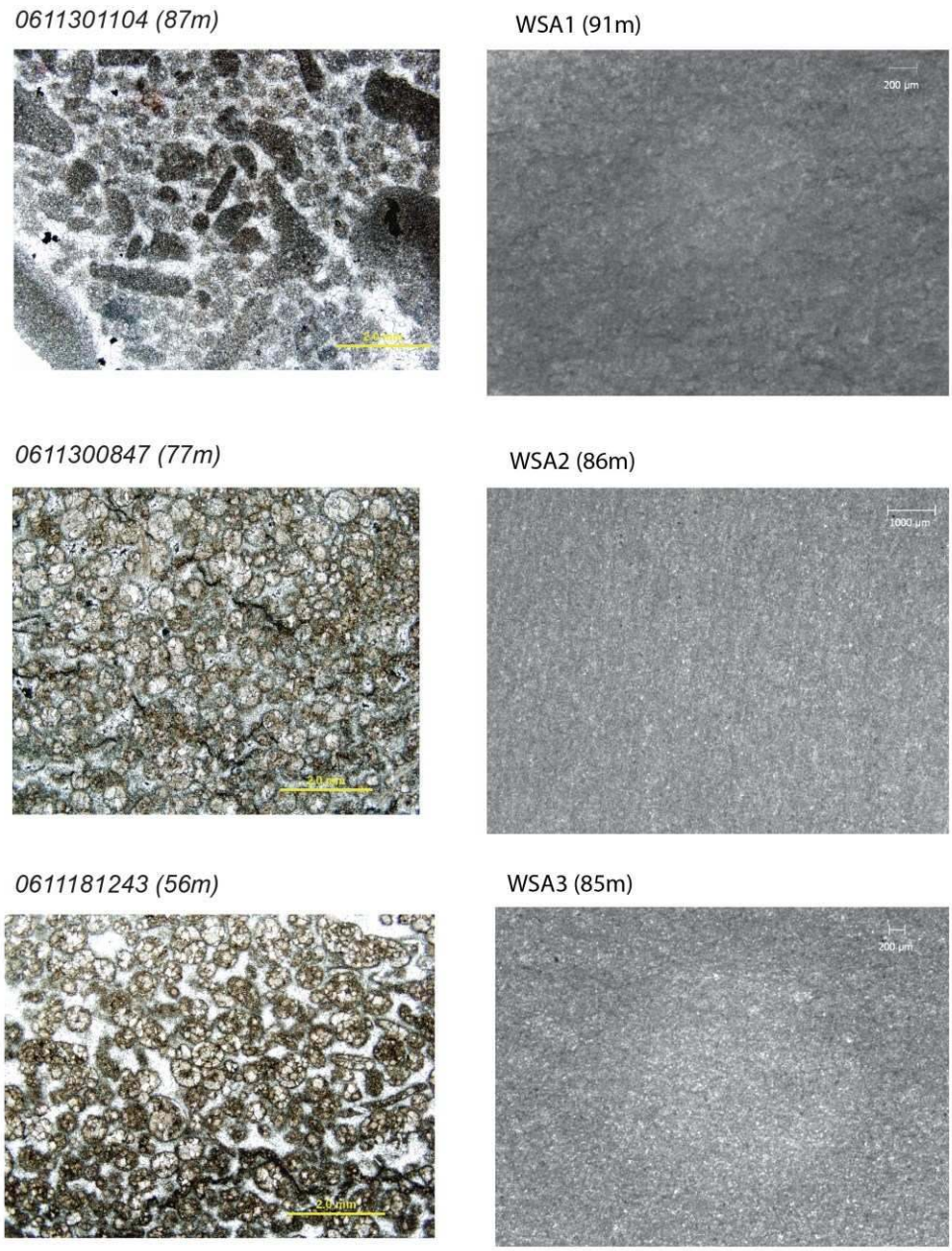

580

581 Fig S1: Examples of thin section images for the Wadi Bih section, WSA transect. WSA samples
582 demonstrate homogeneous micritic texture of samples used for $\delta^{11}B$ analysis. 06- samples are from
583 Maurer et al., (*34*) illustrating grainstones. The lack of compaction of grains and pore filling equant
584 spar cements indicate very early/syn-sedimentary cementation. This fabric is consistent with
585 indicators for supersaturated conditions in this interval, including thrombolites and flat pebble
586 conglomerates, and suggests preservation of the original depositional fabric. Sample heights (m) as
587 in Fig. 2 and Table S1.

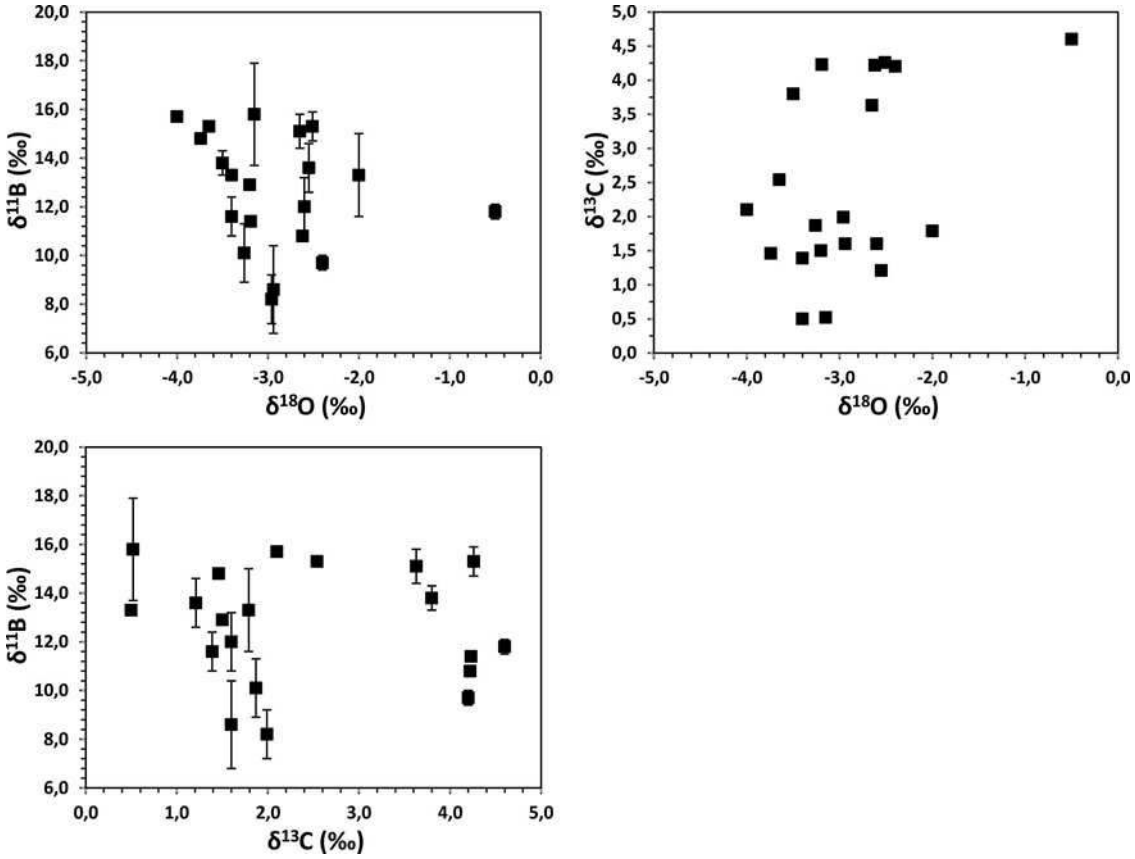

Fig S2: Cross-plots of boron, carbon, and oxygen isotope data for the marine carbonate samples from the Wadi Bih section. No significant correlation can be observed.

2.1 Diagenetic Influences

The PTB interval grainstone is composed of microspheres (a.k.a calcispheres). Microspheres are micritized and cemented with coarse equant spar cement (Fig S1). The lack of compaction of the microspheres suggests that the spar cement was extremely early and probably syn-sedimentary. This is a feature of other grainstones throughout this interval (WSA transect, sample 0611301104). Critically the presence of such well cemented fabrics in the grainstones of this interval would have prevented later stage fluid migration, and hence any late stage dolomitization. The total negative boron isotope excursion at EP2 is recorded across a numberof fabrics and facies, including micrite and the early cemented grainstones. Petrographic analysis

shows the extreme of the acidification event is recorded in fine-grained micrite where textures are very homogenous samples WSA 1, 1B, 2, and 2A (Fig. S1).

Dolomitization in the Wadi Bih section is observed *(14)*, and occurred in two phases where the first phase was fabric retentive syn-sedimentary dolomitization. The second phase of dolomitization leads to the recrystallization of facies where near depositional porosity and permeability had been maintained, i.e. preferentially in non-cemented grainstones. Neither of these phases is classed as deep burial dolomitization (as confirmed by petrography in Figure S1 and the $\delta^{18}O$ data, Table S1). In the Musandam Peninsula the impact of dolomitization on carbon and oxygen isotopes can be seen only in the close proximity to regional faults that provided high permeability pathways for late burial dolomitizing fluids (*43*), which were avoided for this study.

Diagenetic effects were also checked with geochemical tests for selected trace element analyses, using secondary ionisation mass spectrometer Cameca ims 4f at the University of Edinburgh. Diagenetic alteration was explored via Mn/Sr, which is often used as a geochemical indicator of alteration and meteoric diagenesis in ancient carbonates (*44*). While low Mn/Sr has been found in ancient carbonates where there is clear optical evidence for recrystallization (*45*), high Mn/Sr may indicate carbonate precipitation from anoxic waters. In the selected samples, Mn concentration is < 300 μg g^{-1}, Sr concentration ranges from 140 to 1400 μg g^{-1}, and the Mn/Sr ratio is low (< 2), so suggesting no influence of meteoric fluids. The boron concentration for the carbonate rocks is, on average, 1 μg g^{-1} and ranges between 0.2 and 1.7 μg g^{-1}.

Post-depositional alteration, especially meteoric diagenesis and recrystallization, is assumed to decrease the isotopic composition of oxygen, boron and carbon isotopes (e.g. *46-48*). Our selected carbonate samples show the distinct carbon isotope trend found at every PTB section globally and $\delta^{18}O$ values ranging between -0.5 and -4.0‰, indicating no significant deep

burial alteration. All carbon and oxygen isotope data are given in Table S1. No statistically significant correlation between carbon, oxygen and boron isotope data can be observed in our data (Fig. S2).

The replication of the $\delta^{11}B$ across two complementary transects further support the preservation of a primary seawater isotope signature as late stage dolomitization is expected to be highly laterally variable and disrupt the smooth trends seen in the data.

3. Support for a primary Boron isotope signature

3.1 Published $\delta^{11}B$ data

So far, $\delta^{11}B$ data for Triassic carbonates have not been published and only limited $\delta^{11}B$ data, based on low-Mg calcite brachiopod calcite from Oman (Saiwan Fm.), are available for the Permian (Late Sakmarian). Keeping in mind the modern residence time of boron (Ƭ~14 to 20 Ma *(47, 49)*, it is important to note that the range in $\delta^{11}B$ values (10.9±0.9‰ (1σ, n=4), 252.05-252.15 Ma, mid-Changhsingian) overlap with the range in $\delta^{11}B$ values between 10.1 and 11.7‰ of the 285 Ma old brachiopod carbonates (average 10.6±0.‰, 1σ, n=5, (*16*)), which support the primary nature of our boron isotope data.

3.2 Environmental controls on the boron isotope composition

The speciation of boron in seawater is predominantly pH dependent with minor controls from temperature, salinity and pressure (*50)*. In our model we consider a dynamic temperature effect on pK_B to calculate the pH of the seawater from the boron isotope composition preserved in Permo-Triassic carbonate (see SM 4 and 5) however below we evaluate geological evidence to consider whether these variables could drive the trends seen in our data.

647 *3.2.1* Temperature

648 Oxygen isotope data preserved in conodont apatite and low-Mg calcite brachiopods from
649 Permian-Triassic sections in Iran document tropical sea surface temperatures (SST) of 27–33°C
650 during the Changhsingian with a negative shift in $\delta^{18}O$ starting at the extinction horizon,
651 translating into a warming of SSTs to well over 35°C in the mid-Griesbachian (*51*). The results
652 are consistent with SSTs of the South Chinese sections, where a rapid increase in seawater
653 temperature from about 25° to 36°C across the Permian-Triassic section was proposed based on
654 conodont apatite (*6*). Since the dissociation constant of boric acid (pK_B) decreases with
655 increasing temperature (*50*), the proposed increase in SST could drive an increase in the B
656 isotope composition of the carbonates precipitated at the time of global warming and imply an
657 increase in ocean pH, even if ocean pH stayed stable. Using the pK_B data from (*50*), the potential
658 increase in SST at a given pH of 8 would drive an increase in $\delta^{11}B$ of the carbonates by 2‰ and
659 generate an artificial increase of < 0.2 pH units. Consequently, it could be argued that our
660 calculated pH variations are in essence the result of an increase in sea surface temperatures.
661 However, the oxygen isotope pattern (*51*) shows a continuous increase in temperatures across the
662 Permian-Triassic boundary and a thermal maximum in the mid-Griesbachian (~251.85 Ma).
663 Instead our data show a sharp increase in $\delta^{11}B$ and ocean pH in the Late Permian, well before the
664 increase in temperatures at EP1. The slight variability in $\delta^{11}B$ above the PTB, however, could be
665 driven by temperature variations.
666
667
668
669

670 *3.2.2 Salinity*

671 Similar to temperature, the pK_B is sensitive to salinity and increases with decreasing salinity (*52*).
672 To drive significant salinity-associated isotope variations across the Permo-Triassic boundary,
673 drastic changes in salinity (e.g. down to 25 psu compared to 35 psu) would be necessary.
674 However, even if modelled sea surface salinity values for the late Permian indicate generally
675 more saline conditions than present day (*52)*, sea surface salinity values for e.g. Iran and South
676 China still range between 34 and 35 psu (*51)* and will not have a significant effect on our pH
677 calculation. These samples come from an exclusively shallow water environment far from any
678 freshwater input, and so decreases in salinity would not affect our pH interpretations. The
679 depositional environment here ranges between open water ooid shoals to open and restricted
680 lagoon settings, which results in cyclic deposition on the scale of 5m. A shift toward more
681 restricted settings could drive increases in salinity that would affect the $\delta^{11}B$ record; however,
682 these depositional cycles are not on the same scale as the secular trends seen in $\delta^{11}B$.

683

684 *3.2.3 Water Depth*

685 Permo-Triassic seawater pH values have been reconstructed assuming carbonate precipitation at
686 sea surface conditions. Modern bathymetric pH and temperature profiles from the tropics show
687 that pH can decrease by up to ~0.2 units and temperature can drop by 15°C in the first 300 m
688 (*53*). Thus the B isotope composition of carbonates precipitated at greater water depths would be
689 more negative compared to surface precipitates. This potential depth effect is thought to be of
690 minimal influence to the Wadi Bih carbonates due to the exclusively shallow marine (subtidal to
691 intertidal) nature of the succession.

692 Consequently, uncertainties in the $\delta^{11}B$-ocean pH relationship potentially introduced by
693 changes in temperature, salinity, bathymetry or biofacies would not be able to produce the
694 observed B isotope pattern with the sharp increase in the mid-Changhsingian (~252.04 Ma) and
695 the temporary decrease in the mid-Griesbachian (~251.88 Ma), but would be capable of
696 explaining some of the slight variations across the PTB.
697
698 **4. Boron-pH calculations**
699 The boron isotope composition of marine carbonates is used to reconstruct seawater pH values
700 and atmospheric pCO_2 concentrations (e.g. *54-58*). The application of the B isotope system as a
701 proxy for ocean pH is based on the observation that the fractionation factor for isotope exchange
702 between the two different speciation of boron ($B(OH)_3$ and $B(OH)_4^-$) is pH sensitive and
703 produces significant and traceable changes in the isotopic composition of carbonates (e.g. *57*).
704 The carbonate-associated boron isotopic composition $\delta^{11}B_{carb}$ is assumed to be equal to
705 that of seawater $B(OH)_4^-$. The isotopic composition of the two boron species $B(OH)_4^-$ and
706 $B(OH)_3$ is determined by the isotopic fractionation factor $\alpha_{B3\text{-}B4} = 1.0272$ (*59*), the speciation (a
707 strong function of pH, with smaller dependencies on temperature, pressure and salinity), and the
708 overall isotopic composition of seawater $\delta^{11}B_{sw}$. The relationship between pH and $\delta^{11}B_{carb}$ is
709 given by:

710
$$pH = pK_B - \log\left[- \frac{\delta^{11}B_{SW} - \delta^{11}B_{carb}}{\delta^{11}B_{SW} - \alpha_{B3\text{-}B4} \cdot \delta^{11}B_{carb} - 1000 \cdot (\alpha_{B3\text{-}B4} - 1)} \right]$$

711 where the effective dissociation constant pK_B includes the temperature, pressure and salinity
712 dependence. We dynamically calculate pK_B using CO2SYS-MATLAB v1.1 *(60)* (detailed in SM
713 5), which is consistent with the calculation and constants used by (*61*).

714 A prerequisite for reconstruction of past ocean pH values via B isotope data is the
715 knowledge of the primary B isotope composition $\delta^{11}B_{SW}$ of the ambient seawater. The B isotope
716 composition of modern seawater is regarded as being homogeneous with a $\delta^{11}B$ value of 39.5‰
717 *(54)*. However, recent work on Precambrian to Phanerozoic carbonates and evaporites has shown
718 that the B isotope composition of seawater was highly variable in the geological past (*16, 45, 46*)
719 driven mainly by variations in the global boron budget during Earth history (*23*), exceeding the
720 residence time of B in seawater. Permo-Triassic seawater have been calculated based on changes
721 in processes controlling the oceanic boron budget, e.g. oceanic crust production rate and
722 continental boron flux (*16*) and suggests $\delta^{11}B_{SW}$ values of ~38‰ for the early Permian (285 Ma,
723 Late Sakmarian) and ~34‰ just before the PTB (*16*).

724 Given this uncertainty in $\delta^{11}B_{SW}$, we consider a range of values, determined by the
725 overall consistency of the $\delta^{11}B_{carb}$ data with model-derived constraints on the seawater carbonate
726 chemistry and hence pH, resulting in an envelope for the pH calculation. The model scenarios
727 encompass the range of previous estimates for background Early Permian conditions (*13*), which
728 suggest either high pCO_2 with lower pH (CO_2*Hi:* ~10 PAL, pH ~7.5), or low pCO_2 with higher
729 pH (CO_2*Lo:* ~3 PAL, pH ~8). In our model we consider these two scenarios with corresponding
730 seawater boron isotopic composition ($\delta^{11}B_{SW}$ = 34‰ and 36.8‰) required to reproduce the
731 observed $\delta^{11}B_{carb}$ (see SM Section 6 for further details of the model scenarios).

732 We illustrate the effect of uncertainties in $\delta^{11}B_{SW}$ and temperature on pH, and the overall
733 consistency with the $\delta^{11}B_{carb}$ data in Figure S3 and Table S1 (note that the full model described
734 in SM 4 also includes a dynamic calculation of temperature). The lowest $\delta^{11}B_{SW}$ =34‰ and
735 highest pH considered (scenario CO_2*Lo*) is effectively constrained by the model limitation on the
736 highest pH values immediately prior to EP1. The highest $\delta^{11}B_{SW}$ =36.8‰ and lowest pH

737 (scenario CO_2*Hi*) is effectively constrained by the limit of propagated uncertainty (2σf) on the
738 lowest observed $\delta^{11}B_{carb}$ combined with the non-linearity of the B isotope system.

739 An additional uncertainty in interpreting $\delta^{11}B_{carb}$ is introduced by any potential offset or
740 fractionation between seawater borate $\delta^{11}B(OH)_4^-$ and $\delta^{11}B_{carb}$. As shown by (*59*), the laboratory
741 measured fractionation of abiotic carbonate (*61*) shows both an offset relative to that of the
742 artificial seawater, and a shallower slope with increasing pH. As we consider $\delta^{11}B_{SW}$ as a model
743 parameter to be determined, an overall offset is effectively subsumed within this. However a
744 shallower slope than that used here ($^{11-10}K_B$ = 1.0272 [*ref 59*], cf the one given for inorganic
745 carbonates (1.0267; [*ref 62*])) would require a larger pH change for a given observed change in
746 $\delta^{11}B_{carb.}$. Sanyal et al. (*63*) published B isotope values for inorganic calcite precipitates at three
747 different pH conditions - 7.9, 8.3, and 8.6. This same experimental inorganic calcite data and
748 associated estimates of $^{11-10}K_B$ in seawater were also presented by Klochko et al. (*59, 64*). To
749 date, there is no agreement as to the actual deviation of Sanyal's data (*63*) from the now
750 generally-accepted empirical fractionation factor given by Klochko et al (*59*). A best fit value of
751 1.0267 for the inorganic calcite precipitation was given by Pagani et al. (62). But by contrast, the
752 deviation between the inorganic carbonate values and the empirical fractionation appears much
753 bigger in Klochko et al. (*59*) and the best-fit value is given as 1.0260. This increased deviation is
754 explained by the difference in pH scale between natural or artificial seawater used for the
755 calibration experiments, and the experimental seawater pH measured on the (freshwater) NBS
756 scale. Klochko et al. (*64*) tries to address the deviations in $\delta^{11}B$ of inorganic precipitates from
757 empirical calibration studies and concludes that boric acid incorporation may contribute to the
758 ^{11}B enrichment observed in inorganic precipitates, especially at lower pH. They point out,

759 however, that all carbonates precipitated under controlled pH conditions were enriched in ^{11}B
760 relative to seawater borate (*63*).

761 If we use the best fit value (1.0267) given by Pagani et al. (*62*) for the inorganic
762 carbonates (Sanyal et al 2000) instead of the empirical value of Klochko et al. (*59*), then the
763 offset for the majority of the data would be around 0.05 pH units. Visible changes to more acidic
764 values would only appear at the lowermost pH estimates, but would still be less than 0.2 pH units
765 and fall within the general uncertainty. If we take the 1.026 value, the offset would generally
766 increase between ≤0.1 and 0.2 (pH range between ~8.4 and 7.8) but would indeed result in
767 significantly lower pH values of up to 0.5 units for the acidification event.

768 Given the limited amount of experimental inorganic calcite data and this disagreement
769 between the best-fit values, we have taken the simplest approach for the model representation
770 and chosen to use the most generally-accepted empirical fraction factor given by Klochko et al.
771 (*59*).

772

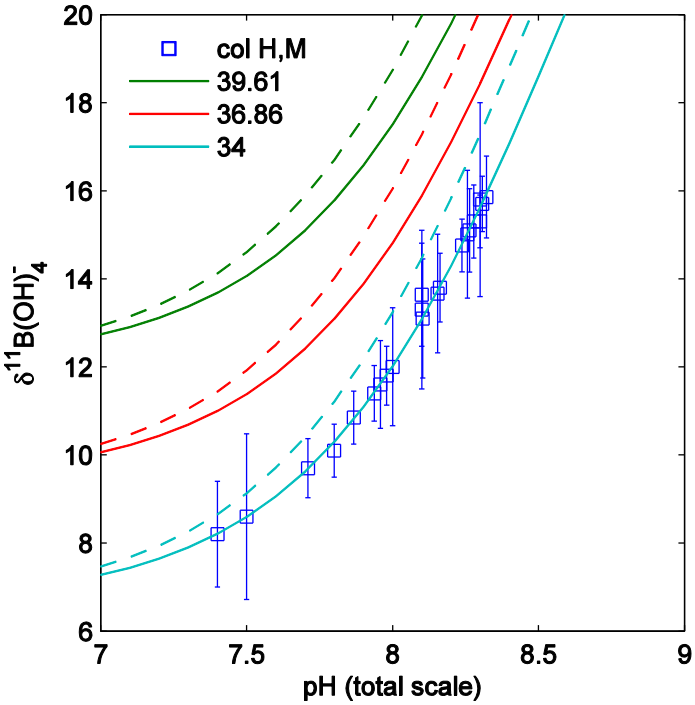

773

774 **Figure S3** Effect of background $\delta^{11}B_{SW}$ and temperature on relationship between $\delta^{11}B_{carb}$ and pH
775 (total scale), for conditions appropriate to low-latitude surface ocean (atmospheric pressure,
776 salinity 35 psu, temperature 25˚C (solid lines) and 35˚C (dashed lines)). Three values are shown for
777 $\delta^{11}B_{SW}$: 39.61‰ (the contemporary value) and two values consistent with the end Permian data.
778 Data points and 2σf errors are overlaid for the $\delta^{11}B_{SW}$ 34‰ case.

779

5. Model Description

5.1 Overview

The overall model structure (shown in Figure S4) is essentially a superset of carbon cycle models previously applied to the end Permian (*65*, *66, 67)*, with additional consideration of the marine sulphur cycle. The model includes a three box ocean model as the minimum needed to demonstrate the effect of the biological pump on vertical DIC gradients and ocean redox state. The model is implemented as a set of coupled differential equations for the time evolution of reservoirs (Table S3), exchanging fluxes according to air-sea exchange, ocean circulation, applied external forcings and perturbations, and the biogeochemical processes described in Table S5. Model constants are defined in Table S4. The model implements an open inorganic carbon cycle, with atmospheric pCO_2 and marine DIC and Alk determined by the feedbacks between land-surface carbonate and silicate weathering and marine carbonate deposition. Oxidative weathering, volcanic degassing, and land and marine organic carbon burial are specified as forcings, as is marine phosphorus and hence productivity.

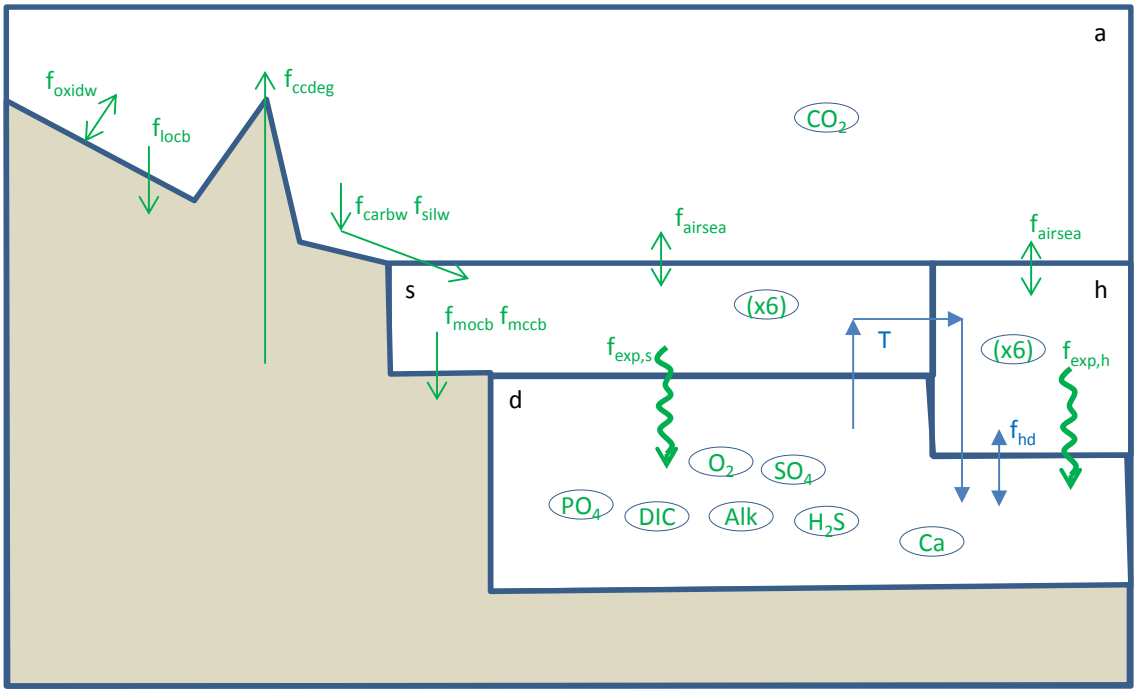

Figure S4 Model schematic. Ocean is represented by three boxes (s, h, d), with well-mixed atmosphere box a. Biogeochemical fluxes are shown in green, ocean circulation in blue. Biogeochemical reservoirs are shown as ovals.

795

796 Table S3 Model reservoirs

Reservoir	Initial size	Description
Atmosphere		
CO_2	eqb[a]	Atmospheric CO_2
Ocean		
$DIC_{(s,h,d)}$	eqb[a]	Total carbon
$Alk_{(s,h,d)}$	eqb[a]	Total alkalinity
$O_{2(s,h,d)}$	eqb[a]	Oxygen
$PO_{4(s,h,d)}$	2.15 µM / kg-sw	Phosphate
$SO_{4(s,h,d)}$	28 mM / kg-sw	Sulphate
$H_2S_{(s,h,d)}$	0	Sulphide
Ca	10.28 mM / kg-sw	Calcium (single reservoir)

[a] set by initial spin-up to steady-state.

797

798 Table S4 Model fluxes, constants, and forcings.

Flux	Model Parameter	Value	Units	Description
crust/mantle				
f_{ccdeg}	k_{12_ccdeg}	varies[a]	mol CO_2 yr^{-1}	Degassing
land surface				
f_{carbw}	k_{14_carbw}	$1.33x10^{13}$	mol $CaCO_3$ yr^{-1}	Carbonate weatherability
f_{silw}	k_{silw}	varies[a]	mol "$CaSiO_3$" yr^{-1}	Silicate weatherability
f_{oxidw}	k_{17_oxidw}	varies[a]	mol C yr^{-1}	Oxidative weathering
f_{locb}	k_{5_locb}	$5x10^{12}$	mol C yr^{-1}	Land organic carbon burial
marine				
	$k_{O\_Asurf(s)}$ $k_{O\_Asurf(h)}$	$0.85x3.6 x10^{14}$ $0.15x3.6 x10^{14}$	m^2	Ocean surface area
	$k_{O\_vol(s)}$	$3.06 x10^{16}$	m^3	Ocean volume
	$k_{O\_vol(h)}$	$1.35 x10^{16}$		
	$k_{O\_vol(d)}$	$1.60 x10^{21}$		
T	k_{O_circT}	20	Sv	Overturning circulation
f_{hd}	$k_{O\_circfhd}$	60	Sv	High latitude – deep exchange
	k_{piston}	0.3	m d^{-1}	Air-sea piston velocity
	$T_{O(s)}$	T_{mean}+ 6.5		Ocean temperature
	$T_{O(d)}$	max(T_{mean}-12.5,2.5)		
	k_{O_sal}	35	psu	Ocean salinity
	$r_{c:p}$	161		Redfield C:P ratio
	$r_{n:p}$	16		Redfield N:P ratio
f_{mccb}	$k_{carbsedshallow}$	varies[a]	mol $CaCO_3$ yr^{-1}	Marine carbonate burial
f_{mocb}	k_{2_mocb}	$5x10^{12}$	mol C yr^{-1}	Marine organic carbon burial

[a] parameters k_{silw}, k_{12_ccdeg}, $k_{carbsedshallow}$ are per-scenario external forcings.

799

800

Table S5 Biogeochemical processes

Flux	Biogeochemical transformation	Stoichiometry							Rate	Description
		$CO_{2(a)}$	DIC	Ca	O_2	P	H_2S	SO_4^{2-}	Alk		
	land surface									
f_{carbw}	$CO_2 + H_2O + CaCO_3 \rightarrow Ca^{2+} + 2HCO_3^-$	-1	2	1					2	Equation (S2)	Carbonate weathering
f_{silw}	$2CO_2 + H_2O + CaSiO_3 \rightarrow SiO_2 + Ca^{2+} + 2HCO_3^-$	-2	2	1					2	Equation (S1)	Silicate weathering
f_{oxidw}	$CH_2O + O_2 \rightarrow CO_2 + H_2O$	1	0	0					0	k_{17_oxidw}	Oxidative weathering
f_{locb}	$CO_2 + H_2O \rightarrow CH_2O + O_2$	-1	0	0					0	k_{5_locb}	Organic carbon burial
	marine										
f_{exp}	$CO_2 + H_2O + xP \rightarrow CH_2OP_x + O_2$		-1	0	$1+ 2r_{n:p}/r_{c:p}$	$-1/r_{c:p}$	0	0	$r_{n:p}/ r_{c:p}$ [a]	see Section 3.2.4	Export production
	$CH_2OP_x + O_2 \rightarrow CO_2 + H_2O + xP$		1	0	$-1- 2r_{n:p}/r_{c:p}$	$1/r_{c:p}$	0	0	$-r_{n:p}/ r_{c:p}$ [a]	see Section 3.2.4	Aerobic remineralisation
	$CH_2OP_x + \frac{1}{2}SO_4^{2-} \rightarrow HCO_3^- + xP + \frac{1}{2}H_2S$		1	0	0	$1/r_{c:p}$	0.5	-0.5	1	see Section 3.2.4	Sulphate reduction
	$H_2S + 2O_2 \rightarrow SO_4^{2-} + 2H^+$		0	0	-2	0	-1	1	-2	see Section 3.2.4	Sulphide oxidation
f_{mccb}	$Ca^{2+} + HCO_3^- \rightarrow H^+ + CaCO_3$		-1	-1	0	0	0	0	-2	$k_{carbsedshallow} x(\Omega_{aragonite}-1)^{1.7}$	Carbonate deposition
	$2H_2S + Fe(OH)_3 \rightarrow FeS_2 + \frac{1}{2}H_2 + 3H_2O$		0	0	-0.5	0	-2	0	0		Pyrite formation and burial
f_{mocb}	$CO_2 + H_2O \rightarrow CH_2O + O_2$		-1	0	1	0	0	0	0	k_{2_mocb}	Organic carbon burial

[a] contribution from nitrate, assumed at Redfield ratio.

5.2 Detailed description

5.2.1 pCO_2 and temperature

Global mean temperature T_{mean} is calculated from atmospheric pCO_2 using the energy balance model as in COPSE *(68, 69),* with solar insolation appropriate for 250 Mya. Marine temperature $T_{O(s,h,d)}$ is calculated from the global mean assuming a fixed high-low latitude temperature difference and minimum temperature of 2.5^{0}C, with $T_{O(s)}=T_{mean}+6.5\ ^0C$ and $T_{O(h,d)}=\max(T_{mean}-12.5,2.5)\ ^0C$.

5.2.2 Land surface weathering, degassing, and organic carbon burial

Land surface weathering is essentially a stripped-down version of that in COPSE (*69*), with carbonate and silicate weathering included but sulphur weathering and the long-timescale sedimentary reservoirs for sulphur and carbon are omitted. Atmospheric oxygen is fixed at the present-day value. Silicate and carbonate weathering are controlled by atmospheric pCO_2 and temperature with functional forms:

$$f_{silw}=k_{silw}\, e^{0.090(T_{mean}-T_0)}[1+0.038(T_{mean}-T_0)]^{0.65}\left(\frac{2\ pCO_2}{1+pCO_2}\right) \quad \text{(S1)}$$

$$f_{carbw}=k_{14\_carbw}\,[1+0.087(T_{mean}-T_0)]\ \left(\frac{2\ pCO_2}{1+pCO_2}\right) \quad \text{(S2)}$$

where $T_0=15\ ^0C$.

Atmospheric CO_2 is consumed, and carbon, alkalinity and calcium supplied to the ocean, according to the stoichiometry defined in Table S5. Volcanic degassing, oxidative weathering, and land organic carbon burial are prescribed as forcings.

613 *5.2.3 Marine circulation and air-sea exchange*

614 Marine circulation is defined by a thermohaline circulation T, and high-latitude – deep
615 exchange f_{hd}. The marine box model includes P, O, DIC, Alk, SO_4, H_2S as per-box prognostic
616 variables, along with DIC $\delta^{13}C$. Marine carbonate chemistry is calculated using a modified
617 version of CO2SYS-MATLAB v1.1 *(60)*, extended to include sulphide alkalinity using the
618 constants tabulated by (*70*). Air-sea exchange of oxygen and CO_2 assume a fixed piston
619 velocity and temperature-dependent solubility.

620

621 *5.2.4 Marine productivity and burial*

622 Productivity and hence the biological pump are controlled by the marine phosphorus
623 circulation. Biomass is produced in the surface ocean boxes, and exported and remineralized
624 in the deep box according to the processes and stoichiometries defined in Table S5.
625 Productivity in the 's' box is specified to consume all phosphorus down to negligible
626 concentration. Productivity in the 'h' box is specified to consume a fraction 0.18 of input
627 phosphorus. Remineralization in the deep ocean box consumes oxygen down to a limiting
628 concentration of 1μM and thereafter reduces sulphate to sulphide.

629 Shallow-water carbonate deposition occurs in the 's' box only and is controlled by
630 aragonite saturation state and a parameter representing a combination of shelf area and
631 calcification effectiveness, ie a 'Neritic' ocean without pelagic calcifiers (*71)*, functional
632 form $k_{carbsedshallow}*(\Omega_{aragonite}-1)^{1.7}$. Ocean carbonate compensation is not included, on the basis
633 this will be small for a 'Neritan' ocean.

634 Marine organic carbon burial from the 's' box and pyrite burial from the 'd' box are
635 imposed as forcings. Given the uncertainties in controls on phosphorus input over the end-
636 Permian interval, the marine phosphorus cycle is semi-closed (i.e. weathering feedback on
637 phosphorus input is not included), with imposed perturbations (forcings) to source/sink

balance (riverine input vs burial) applied as inputs to the 's' box to control phosphorus concentration.

5.2.5 Carbon isotopes

Carbon isotopes are implemented with additional reservoirs for each of atmospheric CO_2 and marine $DIC_{(s,h,d)}$. Air-sea exchange fractionates according to the temperature-dependent equilibrium and kinetic factors determined by Zhang et al. (*72*). Marine export production is at fixed fractionation relative to DIC, with $\delta^{13}C_{exp(s,h)} = \delta^{13}DIC_{(s,h)} - 25$ ‰.

Volcanic degassing, carbonate weathering, and oxidative weathering are assumed to add carbon at fixed fractionations of -4.9‰, 2.65‰, and -25‰ respectively. Atmospheric CO_2 consumed by silicate and carbonate weathering (and added to the ocean 's' box as DIC) is fractionated relative to atmospheric CO_2 according to the freshwater fractionation of Zhang et al. (*72*).

Land and marine organic carbon burial is at fixed fractionation relative to atmospheric CO_2 and marine DIC, with $\delta^{13}C_{locb} = \delta^{13}CO_2 - 19$ ‰ and $\delta^{13}C_{mocb} = \delta^{13}DIC_{(s)} - 25$ ‰. Marine inorganic carbon burial is assumed to not fractionate relative to $DIC_{(s)}$.

5.2.6 Boron isotopes

Carbonate-associated boron isotopic composition $\delta^{11}B_{carb}$ is assumed to be equal to that of seawater $B(OH)_4^-$. Speciation of $B(OH)_4^-$ and $B(OH)_3$ is calculated using CO2SYS-MATLAB v1.1 *(60)*. Isotopic composition is then calculated from speciation $x_{bo4} = [B(OH)_4^-]/[B\ total]$ and seawater $\delta^{11}B_{SW}$ as

$$\delta^{11}B_{carb} = \frac{\delta^{11}B_{sw} - 1000(1 - x_{bo4})(\alpha_B - 1)}{\alpha_B - x_{bo4}(\alpha_B - 1)}$$

with the isotopic fractionation factor $\alpha_B = 1.0272$.

662

663 *5.2.7 Model spinup and steady state*

664 The model pCO_2 steady-state is defined by the imposed degassing rate, organic carbon burial
665 and oxidation, and silicate weathering parameterisations, where these together define a
666 unique value for the steady-state atmospheric pCO2 and temperature where $f_{ccdeg}+f_{oxidw}$ =
667 $f_{silw}+f_{locb}+f_{mocb}$. During spin-up, the ocean chemistry and hence atmosphere-ocean CO_2
668 partitioning adjust (on the silicate weathering timescale of ~100kyr) to a steady-state, with
669 the aragonite saturation state adjusting such that carbonate burial balances inputs from
670 carbonate and silicate weathering.

671

672 *5.2.8 Sensitivity to seawater composition*

673 The Mg and Ca composition of end-Permian seawater (as determined from fluid inclusions)
674 is consistent with that of modern seawater ([Mg] = 53 mmol/kg, [Ca] = 10.3 mmol/kg), but
675 with large uncertainties (*6*). Sulphate concentration may have been much lower than modern
676 values (*73, 74*). We estimate the uncertainties in carbonate system chemistry following the
677 approach of (*75*). We estimate the effect on K_1 and K_2 from model results (*74*) as:

$$\frac{K_1^*}{K_1} = 1 + 0.155\frac{\Delta[Mg^{2+}]}{[Mg^{2+}]_m} + 0.033\frac{\Delta[Ca^{2+}]}{[Ca^{2+}]_m} - 0.019\frac{\Delta[SO_4^{2-}]}{[SO_4^{2-}]_m}$$

$$\frac{K_2^*}{K_2} = 1 + 0.641\frac{\Delta[Mg^{2+}]}{[Mg^{2+}]_m} + 0.071\frac{\Delta[Ca^{2+}]}{[Ca^{2+}]_m} - 0.054\frac{\Delta[SO_4^{2-}]}{[SO_4^{2-}]_m}$$

678 where subscript m refers to modern values and an asterix to end-Permian values. Taking
679 extremal values $[Mg^{2+}]^*/[Mg]_m=0.5$, $[Ca^{2+}]^*/[Ca]_m=2$, $[SO^{2-}{}_4]^*/[\ SO^{2-}{}_4]_m=0.1$, we have
680 K_1^*/K_1=1-0.078+0.033+0.0171=0.972 or $pK_1^*=pK_1+0.012$ (or for $[Mg^{2+}]$ alone,
681 K_1^*/K_1=0.92, $pK_1^*=pK_1+0.035$). For a fixed pCO_2, this implies a corresponding decrease in
682 $[HCO_3^-]$ and hence DIC inventory, or equivalently an increase in pH for the same DIC
683 content. The corresponding effect on K_2 is much larger, K_2^*/K_2=1-

0.32+0.0171+0.049=0.75.We estimate the effect of Mg concentration on the calcite solubility constant K_{sp} using the parameterisation given by (*76*) as:

$$\frac{K_{sp}^{*}}{K_{sp,m}} = 1 - 0.0833\left(\frac{[Mg^{2+}]_m}{[Ca^{2+}]_m} - \frac{[Mg^{2+}]^*}{[Ca^{2+}]^*}\right)$$

which gives K_{sp}*/K_{sp}=1-0.33.

This sensitivity study shows that the uncertainty in K_1 therefore introduces only a small uncertainty in pH (~< 0.03) or equivalently a ~10% uncertainty in DIC inventory relative to pCO_2. The combined uncertainties in K_2, K_{sp} and $[Ca^{2+}]$ are larger, introducing corresponding uncertainties in calcite saturation state. However, within the model employed here, this is effectively absorbed into a rescaling of the parameter $k_{carbsedshallow}$.

6- Model Scenarios

Given the uncertainty in the absolute value of the seawater boron isotope composition (section S4), we consider two scenarios with initial steady-state conditions as in Table S6: scenario CO_2*Hi* uses $\delta^{11}B_{SW}$=36.86, and CO_2*Lo* uses $\delta^{11}B_{SW}$=34. Here ocean pH depends on the combination of atmospheric pCO_2 and carbonate saturation state. Atmospheric pCO_2 (set by the ratio of net carbon sources : silicate weatherability) is tuned to 3 or 10 PAL, encompassing the range of conditions considered by previous model studies *(77, 78, 79)*. Ocean carbonate saturation state is set by carbonate sedimentation efficiency parameter $k_{carbsedshallow}$, which represents a combination of shelf area x deposition rate. A summary of scenarios required to explain the three events in our $\delta^{11}B$ data are given in Table S7 and explored in further detail below.

705 Table S6 Steady-state initial conditions summary

	CO_2*Hi*	**CO_2*Lo***	**Units**	**Description**
Parameters				
k_{12_ccdeg}	$11.80x10^{12}$	$11.80x10^{12}$	mol CO_2 yr^{-1}	degassing
k_{17_oxidw}	$5x10^{12}$	$5.92x10^{12}$	mol C yr^{-1}	oxidative weathering
k_{silw}	$2.40x10^{12}$	$6.60x10^{12}$	mol $CaSiO_3$ yr^{-1}	Silicate weatherability
$k_{carbsedshallow}$	$18.43x10^{12}$	$1.44x10^{12}$	mol $CaCO_3$ yr^{-1}	Marine carbonate burial efficiency
Steady-state conditions				
pCO_2, ppm	2800	845		
T_{mean}	22.18	14.94	^0C	Global mean temp
$T_{O(s)}$	28.7	21.44	^0C	Ocean temp
$\Omega_{arag(s)}$	2.44	6.15		Aragonite saturation, 's' box
pH	7.51,7.46,7.07	8.02, 7.99, 7.60	Total scale	Ocean pH, 's','h','d'
DIC total	$5.53x10^{18}$	$6.01x10^{18}$	mol	
$\delta^{13}DIC_{(s)}$	+3.32	+2.97	‰	
Fluxes				
f_{carbw}	$27.46x10^{12}$	$15.58x10^{12}$	mol $CaCO_3$ yr^{-1}	Carbonate weathering
f_{silw}	$6.80x10^{12}$	$7.72x10^{12}$	mol "$CaSiO_3$" yr^{-1}	Silicate weathering
f_{ccdeg}	$11.80x10^{12}$	$11.80x10^{12}$	mol CO_2 yr^{-1}	Degassing
f_{mccb}	$34.26\ x10^{12}$	$23.30x10^{12}$	mol $CaCO_3$ yr^{-1}	Marine carbonate burial

706

707 Table S7 Overview of scenarios

Event	**Time**	**Scenario**	
		CO_2*Hi*	**CO_2*Lo***
		$\delta^{11}B_{sw}$=36.86	$\delta^{11}B_{sw}$=34
pH rise	252.25 Ma	Marine productivity increase	
	252.05 Ma	Carbonate sedimentation efficiency decrease	
		Pyrite deposition, Carbonate weathering increase	
$\delta^{13}C$ drop, stable pH	252.00 Ma	Land organic carbon burial decrease	
	251.95 Ma	Slow (~50kyr) isotopically light carbon addition.	
Acidification, no $\delta^{13}C$ change	251.88 Ma	Rapid (10kyr) isotopically heavy carbon addition	

708

709

710 ***6.1 Mechanisms for pH rise***

711 The rise in $\delta^{11}B$ at 252.05 Ma corresponds to a rise in pH from 7.5 to 8.0 for scenario CO_2*Hi*,
712 and from 8.0 to 8.3 for scenario CO_2*Lo*. Given the major upheavals in the Earth system at the
713 end-Permian, multiple mechanisms including changes in silicate and carbonate weathering,
714 and marine changes in calcification and due to anoxia may potentially contribute to pH rise,
715 and we use model sensitivity studies to determine potential constraints. We first review
716 evidence for each mechanism, then summarize the model sensitivity studies and propose
717 plausible scenarios involving multiple drivers.

718 *6.1.1 Carbonate weathering*

719 The overall high weathering rates across the Permian-Triassic boundary also imply an
720 increase in carbonate weathering, possibly combined with any direct effect from chemical
721 weathering of eroded clastic material itself.

722 There is also direct evidence for later sea-level regression and subaerial weathering of
723 the shallowest sections of the S. China carbonate platform, coincident with EP1 *(20)* which
724 may contribute to maintaining pH over this interval. To estimate an order of magnitude for
725 enhanced carbonate shelf weathering: 10^{18} mol $CaCO_3$, density 2.8 g cm^{-3} has volume 36,000
726 km^3, or 100m x $3.6x10^5 km^2$, or 1800km of 200km wide shelf; this would provide a
727 weathering flux of 10^{13} mol $CaCO_3$ yr^{-1} for 100 kyr, comparable to the background carbonate
728 weathering rate.

729 *6.1.2 Decrease in calcification effectiveness*

730 Overall global biotic calcification effectiveness is determined by the combination of available
731 shelf area, and local ecosystem-dependent rates. A reduction in area of deposition could be
732 because anoxic/euxinic waters extend onto the shelf bottom precluding those parts from
733 hosting deposition, and/or because there is a sea level change reducing shelf area. The input
734 of clastics prior to EP1 could also reduce carbonate production as a result of ecosystem
735 impacts (*80, 81*).

736 *6.1.3 Productivity-driven ocean anoxia, sulphate reduction, and pyrite burial*

737 Multiple lines of evidence suggest a (large) expansion of oxygen minimum zones prior to the
738 PT boundary, while the deep ocean remains suboxic. These include U isotope evidence for
739 ~6x increase in anoxic fraction (*82)*, extensive pyrite deposition (*83*), and GCM studies (*84*)
740 illustrating the spatial distribution of anoxia.

We represent productivity-driven ocean anoxia by increasing marine phosphorus from the present-day value to 2.3x present (the value used by (*66*). This is achieved by adding phosphorus to the marine 's' reservoir (representing a net excess of riverine input over sediment output) at rate 3.9×10^{10} mol yr^{-1} over the interval 252.15 – 252.05 Ma (cf present-day riverine input $\approx 2 \times 10^{10}$ mol yr^{-1}) (*64*). This results in pCO_2 drawdown as a result of the increased biological pump, and in sulphate reduction leading to ~ 50 μM H_2S in the 'd' box. Note that sulphate reduction increases alkalinity / pH in the 'd' box by $\Delta pH \sim 0.1$, but as the S redox shuttle is completed by sulphide oxidation at the base of the oxic surface box, this has no effect on the pH of the oxic surface ocean.

High rates of pyrite formation are seen at and before EP1 (*83, 85*). Pyrite burial results in a net alkalinity source (*86*). We assume that pyrite deposition is a water-column process, hence is limited by the availability of iron and sulphide. The most limiting factor for the scenarios considered here is iron. To quantify this, we estimate pyrite deposition rate sustainable over a timescale of ~100kyr as $\sim 1.25 \times 10^{12}$ mol FeS_2 yr^{-1}, based on availability of reactive iron Fe_{HR} (in the contemporary oxic ocean, Fe_{HR} total input to the ocean is $\sim 6.8 \times 10^{12}$ mol yr^{-1}, of which only $\sim 1.3 \times 10^{12}$ mol yr^{-1} gets to the deep ocean (*87*). Sulphide availability is determined by anaerobic organic carbon remineralisation in the 'd' box, which is a model-determined fraction of total export production $\sim 10^{14}$ mol yr^{-1}, and is less limiting than iron for the scenarios considered here. This assumes that sulphate for remineralisation (and hence sulphide availability) is unconstrained by marine sulphur availability, ie that the marine sulphate reservoir is drawn down. This is supported by (or at least consistent with) the data indicating low early Triassic marine sulphate, < 4mM (*75, 88*).

764 *6.1.4 Silicate weathering*

765 Anomalously high sediment fluxes across the Permian-Triassic boundary *(80, 81*) imply soil
766 loss and increased exposure of highly weatherable rock surfaces, with increases in both
767 physical and chemical weathering. Early Siberian traps emplacement and an increase in area
768 of weatherable basalt also may contribute to an increase in overall silicate weatherability. The
769 main increase in silicate weathering is seen in the Griesbachian but increases may have
770 accompanied the carbon injection for EP1.

771 *6.1.5 Combined scenarios*

772 We summarize the effect of illustrative perturbations for the separate contribution of each
773 potential driver of pH increase in Table S8. Perturbations were applied to the CO_2*Lo* steady
774 state at 251.95Ma (corresponding to the pH rise seen in the $\delta^{11}B$ data), with effect shown
775 100kyr later (at EP1). The marine carbonate system responds on a timescale of ~10kyr,
776 hence reaches a steady state source-sink balance, however the timescale for land-surface
777 weathering feedbacks is >~100 kyr hence the system does not reach a steady state. The
778 dynamic response is included in the full scenarios.

779 As shown in figure S5, the perturbations fall into two groups. Increases in silicate
780 weatherability and pyrite deposition leave carbonate input rate and calcification output
781 essentially unchanged, hence result in changes to atmospheric pCO_2 at nearly constant
782 saturation state. Changes to atmospheric pCO_2 alone are unable to produce a change in pH or
783 $\delta^{11}B$ as large as that seen in the data without implausibly low pCO_2 and hence temperature,
784 hence these cannot be the sole drivers of pH increase. Reductions in calcification
785 effectiveness or increases in carbonate inputs change both the carbonate system saturation
786 state and atmospheric pCO_2, resulting in a much larger increase in pH for a given decrease in
787 pCO_2. A major contribution from either or both of these mechanisms is therefore required.

788 The results from the perturbations study demonstrate that all mechanisms may
789 contribute to pH rise, with a major contribution from either or both carbonate input and
790 decrease in calcification effectiveness required. Given the most likely case where multiple
791 mechanisms all contribute, we construct scenarios with a decrease in calcification
792 effectiveness as the major component and smaller contributions from pyrite burial and
793 carbonate weathering (Figure S6). The perturbations considered for the two scenarios are
794 summarized in Table S9 and the dynamic response is shown in Figure S6.
795
796
797

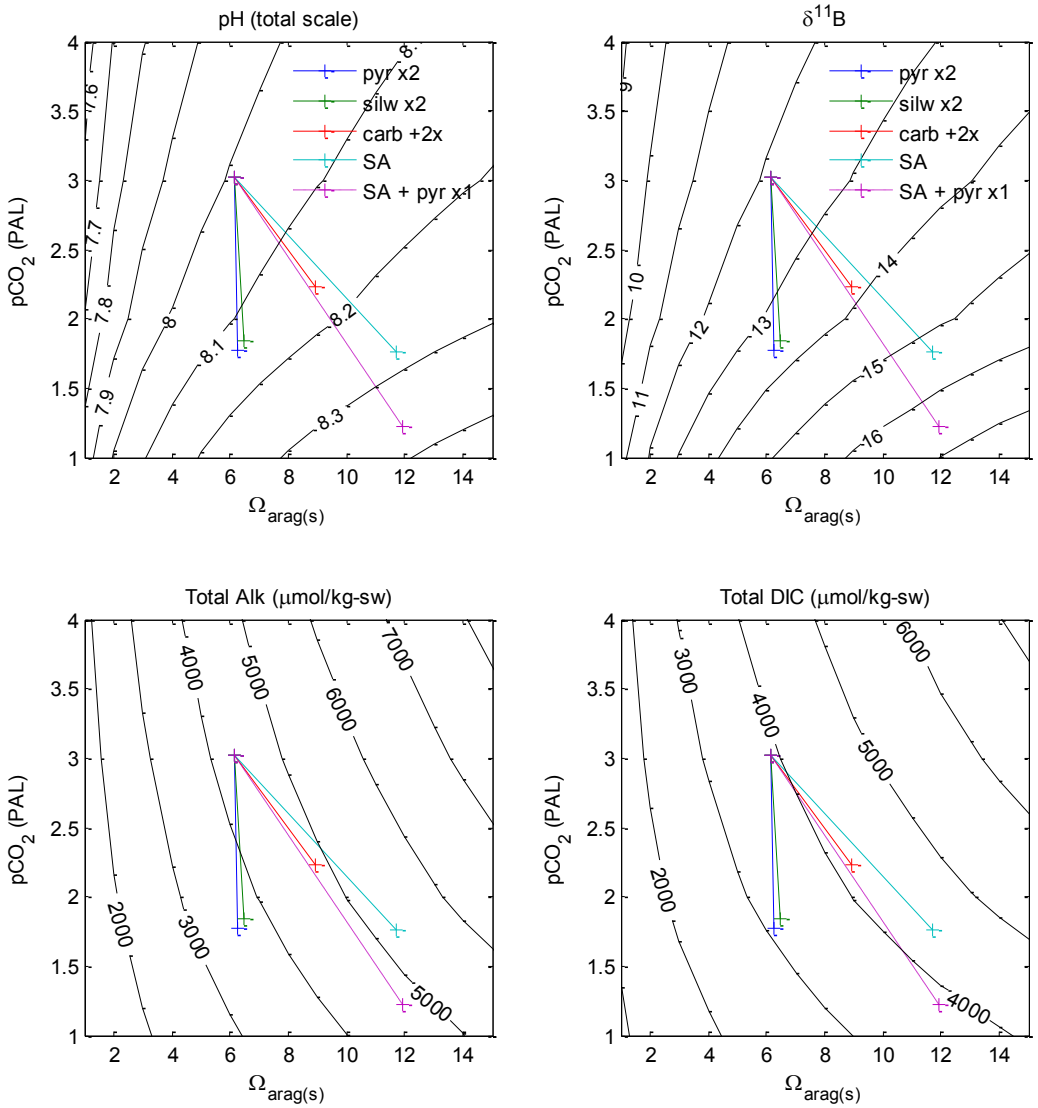

Figure S5 Effect of illustrative perturbations (defined in Table S8) on carbonate system properties for atmosphere and ocean surface (s) box. Contours show carbonate system parameters for a constant temperature of 25 °C, salinity 35 psu, pressure 1 atm, hence do not exactly correspond to the full model results with varying temperature.

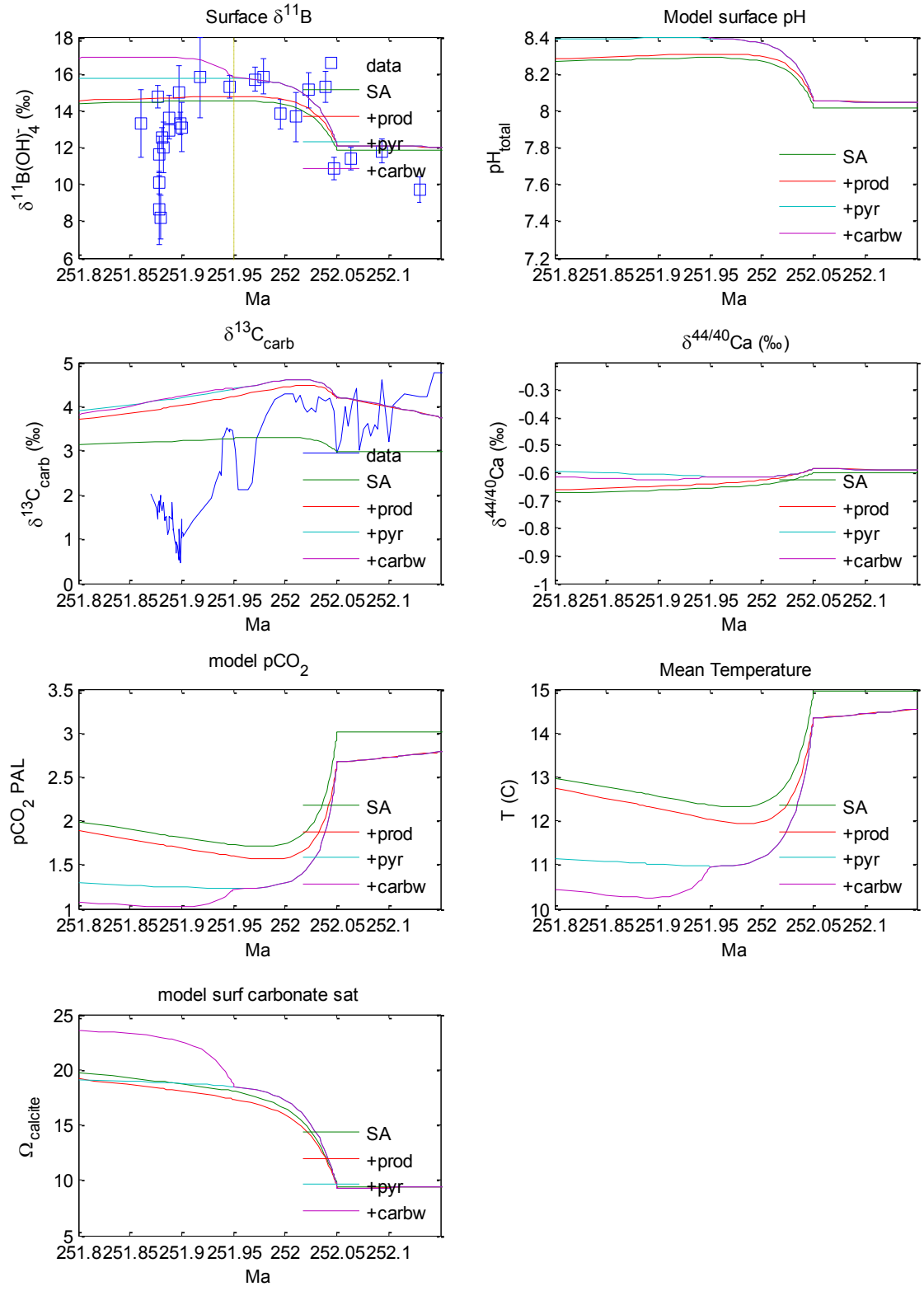

Figure S6 Scenario CO_2*Lo*: Contributions to pH increase. 'SA': effect of calcification effectiveness decrease. '+prod' effect of increased marine productivity and anoxia. '+pyr' pyrite burial, and '+carb' carbonate weathering

802

803 Table S8 Sensitivity study for pH rise mechanisms. Perturbations applied to steady-state CO_2Lo at 252.05Ma, effect shown at 251.95Ma.

Mechanism	Perturbation	$pH_{tot(s)}$	$\delta^{11}B_{(s)}$	$\Omega_{arag(s)}$	pCO_2	T_{mean}	Comments
steady-state CO_2Lo	none	8.02	11.83	6.15	845	14.94	**Error! Reference source not found.**
		Δ	**Δ**	**Δ**	**Δ**	**Δ**	
'calc eff' decrease	$k_{carbsedshallow}$ $14.4x10^{11}$ → $2.47x10^{11}$ (ie x 0.17)	+0.266	+2.72	+5.55	-351	-2.58	
	$k_{carbsedshallow}$ $14.4x10^{11}$ → $1.23x10^{11}$ (ie x 0.085)	+0.36	+3.78	+8.2	-446	-3.39	
pyr deposition	'x1': $1.25x10^{12}$ mol FeS_2 yr^{-1}	+0.083	+0.71	-0.03	-213	-1.39	
	'x2': $2.5x10^{12}$ mol FeS_2 yr^{-1}	+0.155	+1.36	+0.12	-347	-2.46	
	'x4': $5x10^{12}$ mol FeS_2 yr^{-1}	+0.318	+3.062	+0.46	-557	-4.66	~ upper limit from Fe availability
carb input	'+1x': add $15x10^{12}$ mol $CaCO_3$ yr^{-1}	+0.082	+0.77	+1.44	-130	-0.81	+1x = approx 2x background weathering rate. Ocean carb deposition rapidly compensates
	'+2x': add $30x10^{12}$ mol $CaCO_3$ yr^{-1}	+0.147	+1.41	+2.76	-219	-1.44	+2x = ~3x background weath rate
	'+3x': add $45x10^{12}$ mol $CaCO_3$ yr^{-1}	+0.20	+1.97	+3.99	-285	-1.94	+3x = ~4x background weath rate
silw weath increase	x2 k_{silw} $6.60x10^{12}$→ $13.2x10^{12}$	+0.14	+1.19	+0.35	-329	-2.30	'Weatherability': drives pH primarily via pCO2 decrease
	x4 k_{silw} $6.60x10^{12}$→ $26.4x10^{12}$	+0.32	+3.08	+0.57	-588	-5.09	
calc eff + pyr	$k_{carbsedshallow}$ $14.4x10^{11}$ -> $2.47x10^{11}$ 'x1': $1.25x10^{12}$ mol FeS_2 yr^{-1}	+0.37	+3.91	+5.78	-501	-3.98	used for Scenario *CO_2Lo*.
carb + pyr	'+2x': add $30x10^{12}$ mol $CaCO_3$ yr^{-1} 'x2': $2.5x10^{12}$ mol FeS_2 yr^{-1}	+0.28	+3.09	+2.92	-485	-3.79	

804

805

806 Table S9 Summary of pH rise mechanisms included in scenarios *CO_2Hi and CO_2Lo*

	CO_2Hi	***CO_2Lo***
Decrease in calcification effectiveness	$k_{carbsedshallow}$ decrease from 1.8433 x10^{13} to 0.72 x10^{12}	$k_{carbsedshallow}$ decrease from 1.44 x10^{12} to 2.47 x10^{11}
Productivity,anoxia	Increase P linearly to 2.3x, over interval 252.25 – 252.05 Ma	
Pyrite burial	1.25x10^{12} mol FeS_2 yr^{-1} starting at 252.05Ma	
Carbonate weathering	9.7 x10^{12} mol/yr starting at 251.95Ma	

807

808

809

6.2 Sources of carbon and volatiles causing a negative $\delta^{13}C$ excursion or pH excursion

6.2.1 Terrestrial Carbon burial

The effect of destruction of the land biota and a corresponding decline in land organic carbon burial at the PT boundary was first considered by Broecker and Peacock (*89*). We represent this by setting land organic carbon burial to zero at T=251.95Ma, resulting in a drop in $\delta^{13}C_{carb}$ of ≈ 4‰ (comparable to that seen in end-Permian sections), but over timescale of ~100kyr.

6.2.2 Marine Carbon burial

Despite (or because of) ecological shifts to a cyanobacteria dominated ecosystem (*3*), proxy evidence for continued high sediment organic carbon fluxes (*84*) and a vertical $\delta^{13}C$ gradient (*92, 93*) as well as continuing marine anoxia suggests that high marine productivity continues through Permian-Triassic. Interruption to the marine biological pump would result in a short timescale (ocean circulation timescale ~10^3 yr) increase in surface ocean pH and decrease in surface ocean (and hence carbonate) $\delta^{13}C$. This was considered as a mechanism for short-timescale $\delta^{13}C$ fluctuations over the PT interval (*67*). We do not consider this further here as this mechanism results in coupled perturbations to both surface ocean pH and $\delta^{13}C$, and hence cannot be the major driver for the '$\delta^{13}C$ without pH' or 'pH without $\delta^{13}C$' signals. Smaller perturbations (interruptions) to the biological pump may be plausible as a contributor to short-timescale $\delta^{13}C$ signals following EP1.

832 *6.2.3 Siberian traps volcanism and contact metamorphism*

833 In order to bound plausible model scenarios, we review here potential mechanisms for
834 volatile input from the Siberian Traps and summarise constraints on magnitudes and rates,
835 based on (*24, 27, 93*).

836 The Siberian Traps magma area is estimated as 2.5 – 5x10^6 km^2 and volume >
837 2x10^6 km^3. This intruded into the Tungska sedimentary sequence, which reaches 12.5 km in
838 thickness and includes. ≈2.5 km of Cambrian evaporites containing abundant limestone,
839 halite, dolomite and anhydrite (*24, 27*), coal deposits, as well as Neo-Proterozoic
840 petroleum-bearing shale and carbonate. Intrusion of magma into the sediments resulted in
841 abundant sills and dykes with accompanying contact aureoles, and explosively-generated
842 pipes. The igneous province is estimated to contain approximately 50% intrusive dykes and
843 sills, 30% basalt lava flows, and 20% pyroclastic material (*94, 95*).

844 The volume of sediments affected by contact metamorphism is estimated (*27*) from
845 a sill area of 2x10^6 km^2, thickness 200m, generating a contact aureole of thickness 400m.
846 This results in potential release of 0.8-2.3x10^{18} mol C (as isotopically light methane and
847 CO_2) from metamorphic degassing of organic carbon (assuming the TOC weight percent
848 reacted is 0.5 – 1.5%), over a timescale ≈50kyr. In addition, pipes (each with source region
849 ≈5 km^3) could release 0.1 – 0.3x10^{18} mol C over ≈6.5 kyr. Intrusion into carbonates could
850 release comparable quantities of isotopically-heavy CO_2 via calcsilicate formation and
851 decarbonation of dolomite into periclase and calcite, and intrusion into anhydrite could
852 release comparable quantities of S as SO_2 (*96*). Interaction between petroleum-bearing
853 inclusions and host rock salt could in addition generate halocarbons, estimated at 1-3x10^{17}

854 mol CH_3Cl (*35*). Intrusion into coal-seams could result in explosive interaction resulting in
855 large-scale coal combustion (*93*).
856 The Siberian Traps magmas contain anomalously high quantities of S, Cl, F (*27*),
857 estimated to result in total intrusive and extrusive degassing of 0.2-0.25x10^{18} mol S, 0.1-
858 0.25 x10^{18} mol Cl, and 0.4-0.7 x10^{18} mol F (*31*). The ultimate source of these volatiles is
859 likely to be assimilation from sedimentary host rocks.
860
861 *6.2.4 Carbon injection perturbations*
862 Given the episodic nature and likely variability in isotopic composition of carbon additions
863 from Siberian Traps volcanism and contact metamorphism, we consider size, rate, and
864 isotopic composition of carbon additions via sensitivity studies within plausible ranges.
865 The effect on $\delta^{13}C_{carb}$ of a carbon addition of isotopic composition $\delta^{13}C_{carb}$ is given
866 approximately by mass-balance with the surface (atmosphere and ocean) carbon reservoirs
867 (*78, 79*). The effect on pH is additionally dependent on the rate of addition. We show in
868 Table S10 model results for combinations of addition size, isotopic composition and rate,
869 constrained to result in $\delta^{13}C_{carb}$ = -3 ‰, demonstrating the additional non-linear effect of
870 land-surface weathering feedbacks ('land carbonate compensation').
871 The decline in $\delta^{13}C_{carb}$ over the P-T boundary is faster than can be accounted for by
872 a decrease in land carbon burial alone, implying an additional pulse of isotopically light
873 carbon contribution ~-2‰ to the decline. We show in Figure S7 the constraints from the
874 $\delta^{11}B$ data on carbon additions over the 50kyr interval 251.95 – 251.90 Ma. The results
875 demonstrate that providing the rate of carbon addition is relatively slow as here, the pH

876 constraints are in fact relatively weak, and are consistent with a range of input isotopic
877 compositions $\delta^{13}C_{inj}$.

878 Table S10 Carbon injection perturbations, constrained to result in $\delta^{13}C_{carb}$ = -3 ‰ when
879 applied to steady-state condition CO_2*Lo*

Size (mol C)	**Duration**	**Rate (mol / yr)**	**$\delta^{13}C_{inj}$**	**Δ pH**
$4.75x10^{17}$	10^5 yr	$4.75x10^{12}$	-50	-0.07
$2.47x10^{18}$	10^5 yr	$2.47\ x10^{13}$	-10	-0.28
$3.32x10^{17}$	10^4 yr	$3.32\ x10^{13}$	-50	-0.18
$1.75\ x10^{18}$	10^4 yr	$1.75\ x10^{14}$	-10	-0.64

880

881 The acidification event at ~251.89Ma requires a rapid addition of carbon on a timescale ≤
882 10 kyr, with an isotopic composition $\delta^{13}C_{inj}$≈0 ‰ in order to leave $\delta^{13}C_{carb}$ unaffected, and
883 size ≥ $2x10^{18}$ mol in order to produce a sufficient decline in pH and $\delta^{11}B$ (Figure S8).
884 Larger (or more rapid) carbon additions produce relatively little additional response in
885 ocean pH, as the majority of the input carbon remains in the atmosphere, and the response
886 of the $\delta^{11}B$ is also non-linear at low pH. The rate of the inferred carbon addition is ~3 times
887 the estimates above for organic carbon from the combined effects of sills ($0.16 – 0.4\ x10^{18}$
888 mol C over 10 kyr) and pipes ($0.1 – 0.3\ x10^{18}$ mol C over ~6.5 kyr), but is not unreasonable
889 given the carbonate carbon source and large uncertainties in these estimates.

890

891 *6.2.5 SO_2 injection perturbation*

892 Contact metamorphism of evaporites resulting in large SO_2 release could potentially also
893 contribute to the acidification event. Quantitatively the effect (per mol) on ocean pH is

894 approximately twice that of a carbon addition, and given the relative abundance of
895 evaporites to carbonates is therefore likely to represent a smaller contribution to
896 acidification.

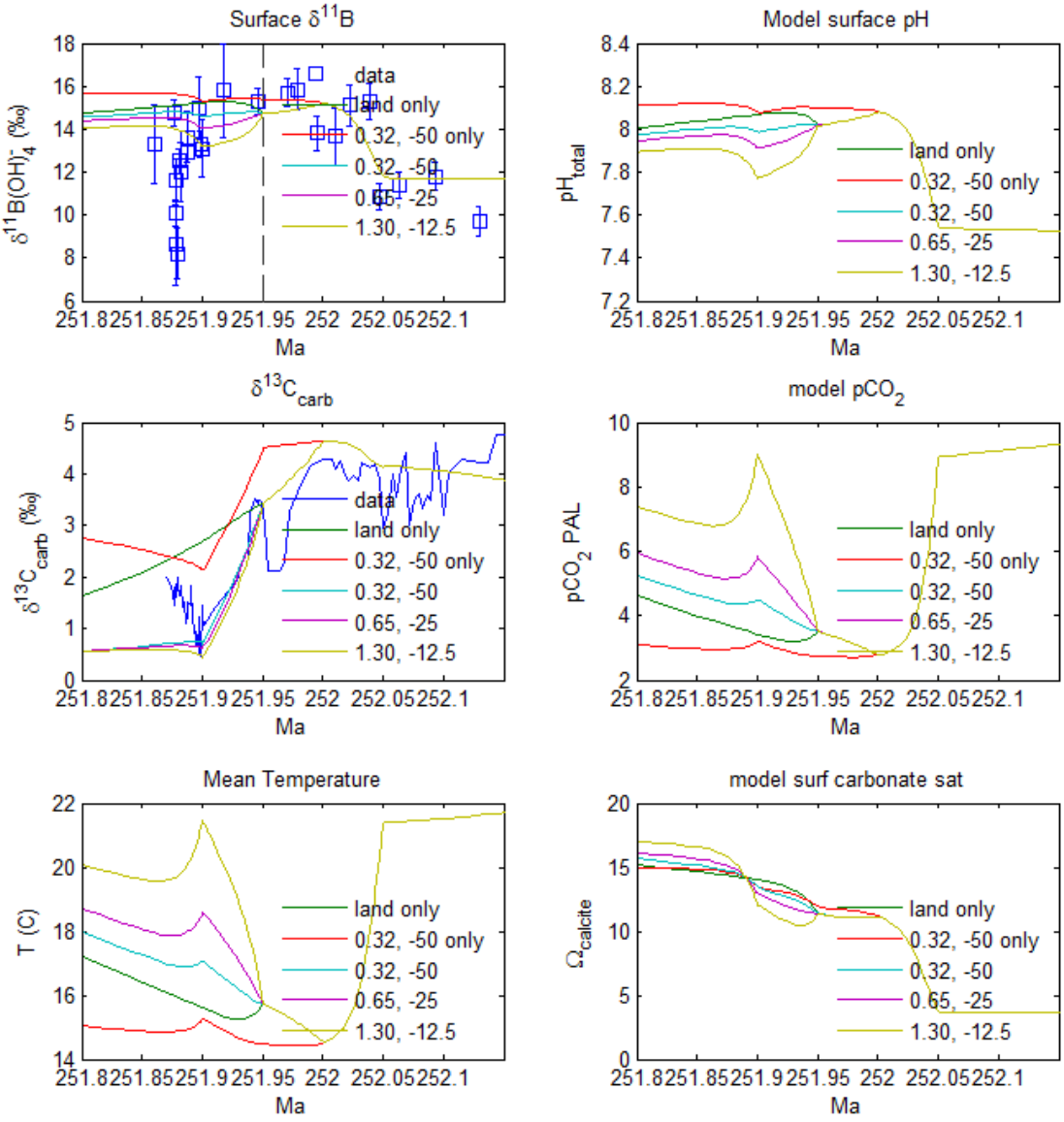

Figure S7 Effect of changing size and isotopic composition of CO_2 input perturbations applied to scenario *CO_2Hi* over 50kyr interval 251.95 – 251.90 Ma. 'land only' shows the effect of interruption in land organic burial,'0.32. -50 only' shows the effect of carbon addition only. Other lines show combined effect of land burial and carbon addition. Perturbations are constructed to result in $\delta^{13}C_{carb} \approx -2$ ‰, and correspond to inputs of: 0.32×10^{18} mol / -50 ‰; 0.65×10^{18} mol / -25 ‰; 1.30×10^{18} mol / -12.5 ‰

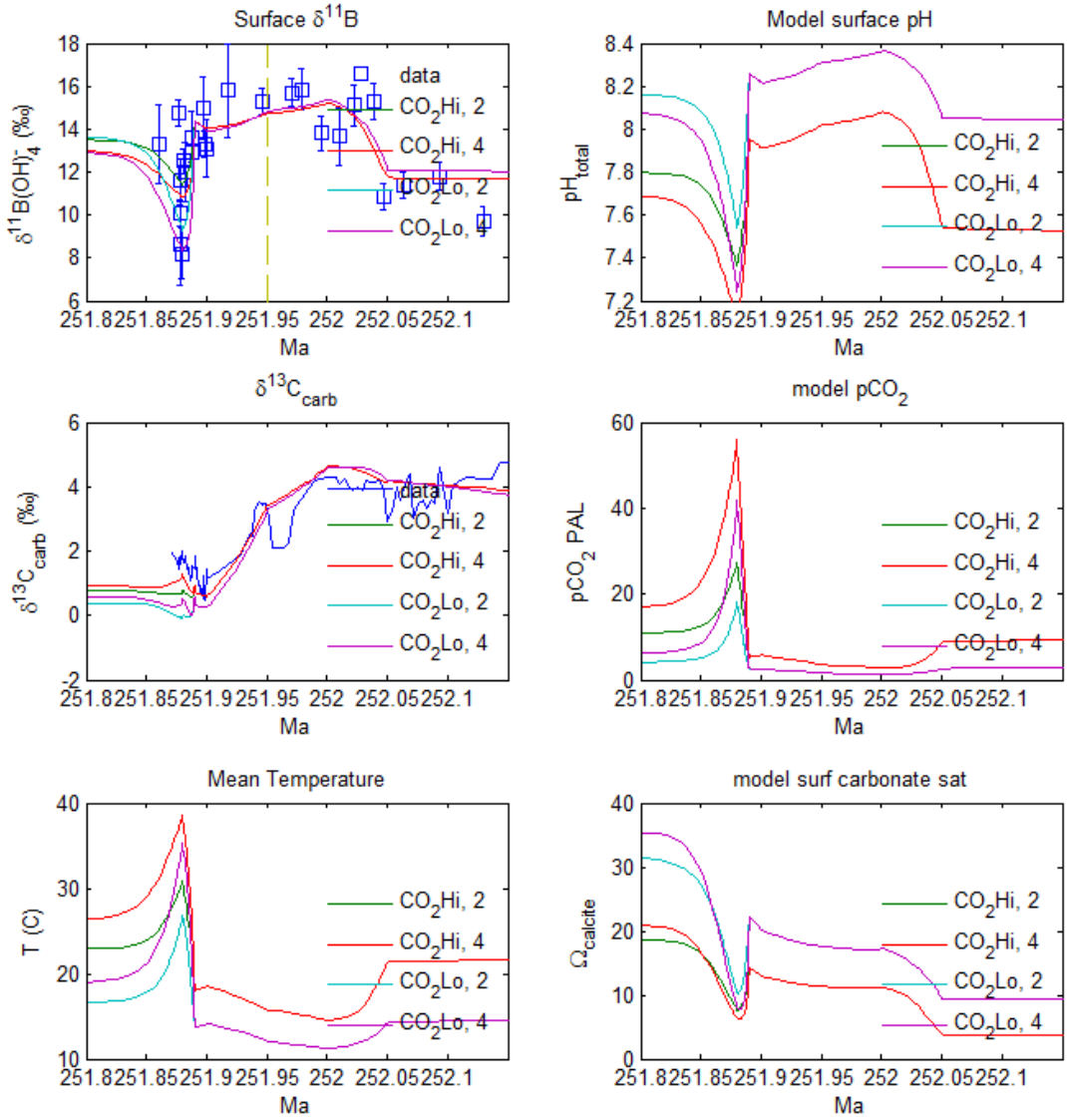

Figure S8 Effect of changing size of CO_2 input perturbations applied to scenarios *CO2Hi* and *CO2Lo* over 10kyr interval 251.89 – 251.88 Ma. Perturbation sizes are $2x10^{18}$ mol and $4x10^{18}$ mol. Isotopic composition is 2.65 ‰, ie equal to that of sedimentary carbonate.

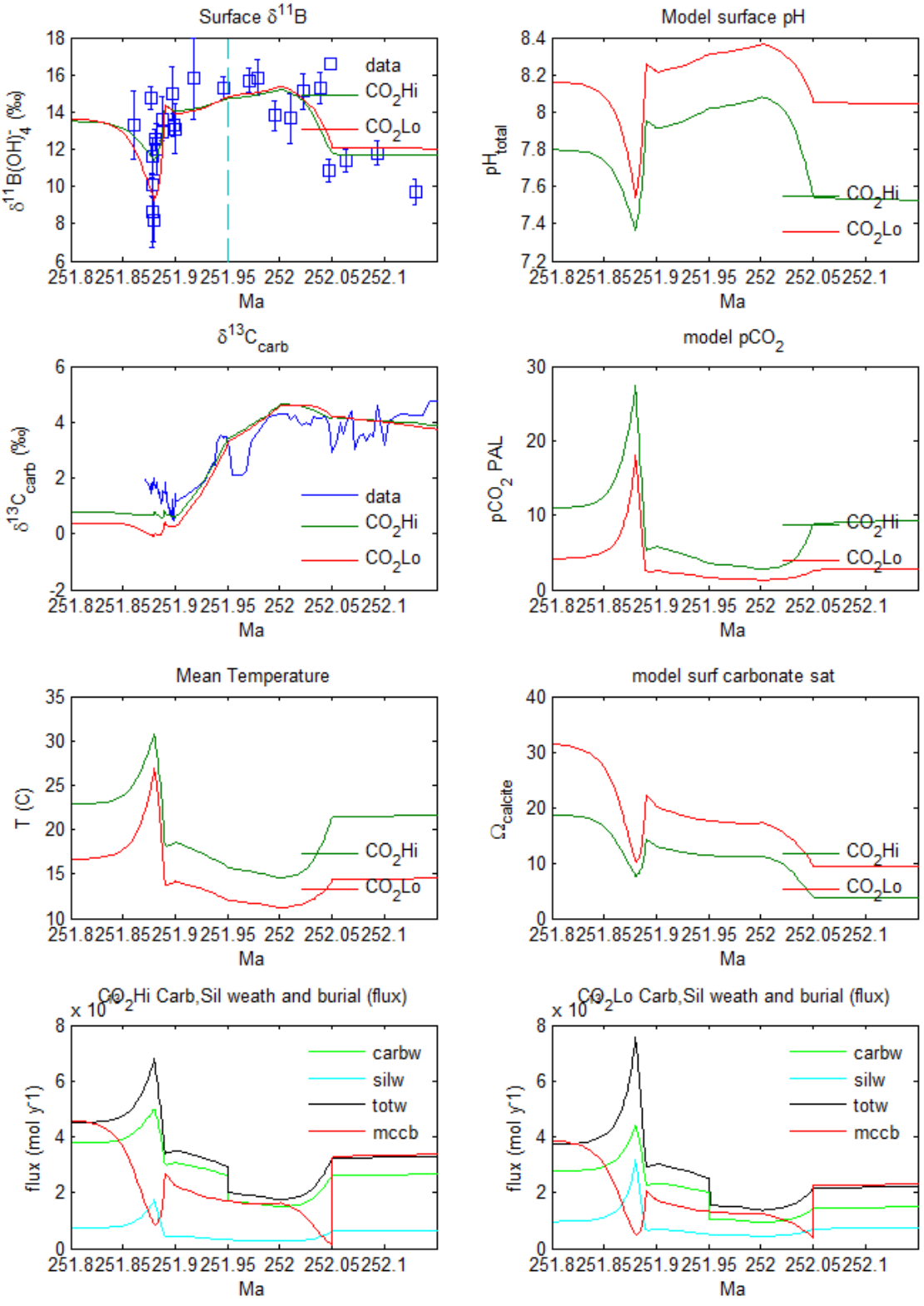

Figure S9 Additional model output for CO_2 scenarios shown in main paper Figure 3. Weathering fluxes are shown for scenario CO_2Lo only.

899